

FOURIER ANALYSIS OF CONDUCTION ELECTRON VELOCITIES BY
ULTRASONIC WAVES IN THE NOBLE METALS

BY

MOSES EGENE ADAH, B. Sc., M.Sc.

DISSERTATION

Presented to the Faculty of the Graduate School of
The University of Texas at Austin
in Partial Fulfillment
of the Requirements
for the Degree of
DOCTOR OF PHILOSOPHY

THE UNIVERSITY OF TEXAS AT AUSTIN

January, 1973

ACKNOWLEDGMENT

I am particularly indebted to my supervising professor, Dr. J. D. Gavenda, for his constant guidance and encouragement throughout the period of investigation which made this work possible.

I am also grateful to Dr. P. R. Antoniewicz for helpful discussions concerning theory and data interpretation, and Dr. L. T. Wood for the use of his computer program (which is based on Halse's function for the Fermi surfaces of the noble metals).

My thanks go to J. K. McGuire and his staff for liquefaction of the helium used in the experiments and for technical advice on low temperature techniques. I would also like to thank John England and his staff, especially Charles Warlick, for the construction of the electronic gate and for improving the pulsed oscillator. Likewise, my thanks go to G. R. Wittig and his staff for the maintenance of the technical equipment used in the experiments. Finally, I am grateful to S. J. Chang and J. P. Masson for their help with experiments.

I am grateful to the African-American Institute for granting me an African Graduate Fellowship for the period of my graduate study.

This work was supported by grants from the National
Science Foundation.

M. E. A.

The University of Texas at Austin
Austin, Texas
January, 1973

TABLE OF CONTENTS

CHAPTER	PAGE
I. Introduction	1
A. The Magnetoacoustic Technique	1
B. Purpose of the Present Work	2
II. Theory	4
A. Theory of the Magnetic-Field Dependence of Ultrasonic Attenuation in Metals	4
1. Development of the Theory	4
2. Methods of Calculating the Attenuation	6
B. Resonances	9
1. Geometric Oscillations	9
2. Cyclotron Resonance and Quantum Oscillations	11
3. Open-Orbit Resonances	11
III. Numerical Calculation of Open-Orbit Resonances	13
A. Theory	13
B. Numerical Calculations	19
IV. Experimental Procedures	24
A. The Ultrasonic Technique	24
B. Sample Alignment in the Magnetic Field	26

C.	Crystal Samples	27
D.	Oxidation-Annealing	29
V.	Experimental Results	34
A.	Introduction	34
B.	Copper Measurements	36
C.	Silver Measurements	36
1.	Symmetry and Determination of Alignment	36
2.	Compressional Waves Propagating along $[\bar{1}01]$	37
3.	Shear Wave Data	44
a)	Primary Open-Orbit Resonances	44
b)	Secondary Open-Orbit Resonances	49
D.	Gold Measurements	53
VI.	Discussion and Interpretation of Results	56
A.	Shear Wave Results	56
B.	Compressional Wave Results	86
VII.	Summary and Conclusions	87
Appendix A.	Pippard's Results for the Attenuation Coefficient	90
Appendix B.	Mertsching's Results for the Attenuation Coefficient	94

Appendix C. Further Details of the Program Orbit . .	96
Bibliography	99
Vita	

CHAPTER I

INTRODUCTION

A. The Magnetoacoustic Technique

Experimental and theoretical evidence during the middle fifties indicated that, in pure metals at liquid helium temperatures, the attenuation of ultrasonic waves is caused by the direct interaction of the conduction electrons and vibrations of the lattice.¹⁻⁵ In particular it was found that, if the electron mean free path is greater than the ultrasonic wavelength, the attenuation of the sound wave may show an oscillatory dependence on the strength of an externally-applied magnetic field. This phenomenon is known as the "magnetoacoustic effect."

The first evidence of ultrasonic attenuation by conduction electrons was obtained from experiments on superconductors by Bömmel and Olsen¹ in 1953, and later by Bömmel² and independently by Mackinnon³ in 1954. Mason⁴ and Morse⁵ immediately proposed different theories to account for this effect. In 1955 Pippard⁶ extended Morse's semiclassical calculation into a general theory for the attenuation of ultrasound in a free-electron gas. The first indications of an oscillatory behavior of the attenuation in an externally-applied magnetic field were seen by Bömmel² in 1955. This

effect was given a geometrical interpretation by Morse⁸ and later by Pippard⁹ as arising from a matching of electron orbit diameters to the sound wavelength. These geometrical oscillations were also seen in experiments by Morse and his group in polycrystalline and single crystal copper^{11,12}. The periods of the oscillations of the attenuation with magnetic field can be related to the momenta of certain groups of electrons and hence provide the means with which the Fermi surfaces of many metals have been mapped. Thus ultrasonics has been found to be a useful technique for studying the electronic properties of metals.

In addition to the geometrical oscillations, other resonance effects have been seen experimentally. These will be reviewed in a later chapter as well as their theoretical treatment.

B. Purpose of the Present Work

Most transport experiments measure average properties of all conduction electrons. In the present work, we use open-orbit resonances to select a band of electrons (open orbit electrons) for a careful study of scattering times, effective force on electrons (self-consistent electric field, collision drag, deformation potential), and Fermi velocity.

The literature on magnetoacoustic attenuation to date indicates lack of consistent agreement between experiments

and theory on some resonance effects. In particular, there has not been any consistent study of the relationship between the amplitudes of the subharmonics of open-orbit resonances. The purpose of the present work is to compare calculations of [111] and [010] open-orbit resonance amplitudes in copper, silver, and gold for a simple phenomenological model using the Fourier components of conduction electron velocities with experimental open-orbit resonances obtained with shear waves.

CHAPTER II

THEORY

A. Theory of the Magnetic-Field Dependence of Ultrasonic Attenuation in Metals

1. Development of the Theory

The first calculations of the attenuation of ultrasonic waves by conduction electrons were those of Morse⁵ and Mason⁴ in explaining the experimental results of Bömmel². They obtained similar results for $q\ell \ll 1$: $\alpha \sim q^2\ell$, where $q = 2\pi/\lambda$, λ is the sound wavelength and ℓ is the electron mean free path. The result for $q\ell \gg 1$ ($\alpha \sim q$) was obtained by Morse⁵ using a quantum mechanical treatment of the problem in which the sound wave was treated as a perturbation of the lattice potential.

The general theory of ultrasonic attenuation for metals in the presence of a magnetic field was worked out by Pippard⁶ in 1955 using a free electron model. He obtained results for compressional and shear waves for the case of arbitrary $q\ell$ using the kinetic device of following a single electron through the lattice and calculating the attenuation from the mean energy gain of the electron per unit time. Holstein¹⁰ used a more rigorous mathematical approach and

obtained results similar to those of Pippard. Holstein's method is the calculation of the electron velocity distribution and hence the electron currents and densities by the solution of the Boltzmann transport equation. The electron currents and the densities in terms of the electric field associated with the sound wave are combined with Maxwell's electromagnetic equations to give a self-consistent scheme. The sound attenuation is obtained by the computation of a dissipative force due to the electrons which acts upon the impressed sound wave. Pippard's and Holstein's methods have become the most general approach to the problem of calculating ultrasonic attenuation by conduction electrons in a crystal lattice.

The first attempt to incorporate the effect of an externally applied magnetic field in the calculation for general $q\ell$ was made by Rodriguez¹³. His method was revised and extended by Kjeldaas and Holstein¹⁴ for the case of propagation perpendicular to the field, and by Kjeldaas¹⁵ for the case of propagation parallel to the field. The most complete free-electron calculation of the magnetic-field dependence of ultrasonic attenuation was made by Cohen, Harrison, and Harrison¹⁶ in 1960. Their results contain most of the essential basic features, such as the various resonance effects, which are seen in experiments.

Pippard¹⁷ made the first general calculations of

the attenuation for real (non-free-electron) metals in the presence of a magnetic field for the case $\vec{q} \perp \vec{B}$. Pippard used a semi-classical, deformational approach while Gurevich¹⁸ made similar calculations using a model developed by Akhiezer et al¹⁹. Other workers^{20,21,22,23} have made various contributions to the problem. Kleinman^{27,28} has recently completed a model calculation for the case of $\vec{q} \parallel \vec{B}$, while Mertsching^{24,25,26} has written a general review of the calculations in three separate papers. Mertsching's results are in close agreement with those of Pippard and also incorporate the detailed investigations of specific cases by Gurevich and his co-workers such as high field anisotropies. A review of Mertsching's and Pippard's general results will be given in Appendices A and B, respectively, while Pippard's approach will be used as the basis for calculating the attenuation by open-orbit electrons which will be developed in a later chapter.

2. Methods of Calculating the Attenuation

When a sound wave propagates through a metal, the ions undergo periodic displacements from their equilibrium positions and small strains are set up in the lattice. As a result, the Fermi surface is deformed in proportion to the strains and the energies of the conduction electrons are changed. Although collisions of the electrons with thermal phonons, impurities, and lattice defects tend to move the

electron distribution to equilibrium, the process is never quite complete, so that the electrons have an excess energy in the presence of the sound wave. Part of this energy is fed back into the sound wave and the rest is dissipated by Joule heating of the lattice, resulting in a net attenuation of the sound energy.

The changes in the Fermi surface can be expressed by introducing a vector deformation parameter \underline{K} so defined that the effect of a deformation is to move the Fermi surface normal to itself by an amount $\underline{K} \cdot \underline{\epsilon}$, where $\underline{\epsilon}$ represents the strain (i.e., the dilation, compression, or shear caused by the sound wave). The deformation parameter is a function of the strain axes chosen and also varies with the position on the Fermi surface. The deformation parameter \underline{K} plays a central role in Pippard's and Mertsching's treatments of the sound wave attenuation.

Pippard's method is the kinetic approach of following the electron through the lattice and investigating each force that can cause the electron to depart from the Fermi surface. The displacement of the Fermi surface is calculated from these forces. The electron current densities and hence the attenuation can then be obtained.

Mertsching adds the excess electron energy $\underline{K} \cdot \underline{\epsilon}$ due to the sound wave to the equilibrium Hamiltonian for the electrons and transforms to a coordinate system fixed in the

moving lattice. He solves the Boltzmann equation for the electron distribution function in the presence of a sound wave, using a Green's function method. Then the average force of the electron acting on the lattice is computed by varying the Hamiltonian with respect to the ion displacements from equilibrium and averaging over the electron distribution. The attenuation is obtained from this electron-ion force.

The presence of a magnetic field \vec{B} forces the electrons into motion around the Fermi surface. If the field is along the z-axis, the electron moves along a constant energy surface defined by planes $\vec{k}_z = \text{constant}$. The real space electron orbits can be obtained by Onsager's theorem²⁹ and are found to have the same shape as \vec{k} -space orbits, but scaled by a factor $\hbar c/eB$ and rotated through $\pi/2$.

The results of detailed calculations by Pippard and Mertsching using the methods outlined above are given in Appendices A and B for comparison. Their results are generally in close agreement and contain all the basic features such as the various resonance conditions, but they also contain other features such as the high field effects which could not be explained on the basis of the free-electron model of CHH¹⁰.

B. Resonances

The path of an electron in a lattice can be closed or open depending on the topology of the Fermi surface and the direction of the applied static magnetic field. Various types of periodic oscillations and resonances can occur in the attenuation coefficient whether the electrons are traveling on closed orbits (e.g., geometric oscillations, cyclotron resonances, and quantum oscillations), or on open orbits (e.g., open-orbit resonances).

1. Geometric Oscillations

Geometric oscillations come about from a matching of some real space orbit dimension to the sound wavelength. The condition can be expressed as

$$D = (n+\gamma)\lambda, \quad n=1,2,3,\dots \quad (2-1)$$

where D is the real space orbit dimension in the direction of sound propagation vector \vec{q} , and λ is the sound wavelength. The phase correction factor γ has values from 0 to $3/8$ for various convex orbit shapes, and corresponding negative values for orbits of concave nature^{26,30,31}. In \vec{k} -space

$$D = \hbar P_0 / eB, \quad (2-2)$$

where P_0 corresponds to the \vec{k} -space open orbit dimension (which is perpendicular to the direction of D in the same

k_z plane). As the magnetic field increases, the real space orbit dimension decreases and the attenuation goes through a series of maxima and minima until \tilde{B} becomes too large to satisfy (2-1). The lowest field at which a peak can occur depends on the electron mean free path, and the range can be defined as $q\ell \gtrsim qD \gtrsim 1$. From (2-1) and (2-2) we see that the geometric oscillations are periodic in $1/B$:

$$\Delta (1/B) = (e\lambda/hc) P_0^{-1} \quad (2-3)$$

Thus the period of a particular series of geometric oscillations can be used to determine the dimension P_0 of the Fermi surface.

We must add that every closed section of the Fermi surface perpendicular to \tilde{B} contributes geometric oscillations of a characteristic period, but the effects tend to cancel out except for those orbits with extremal values of P_0 . However, it has been pointed out¹⁷ that non-extremal cross-sections of the Fermi surface may also produce observable oscillations if the stationary phase points of the orbit are near regions of contact with Brillouin zone boundary, where the deformation potential and cyclotron mass are large.

2. Cyclotron Resonance and Quantum Oscillations

Cyclotron resonances can occur when the cyclotron frequency ω_c ($\omega_c = eB/cm_c$) becomes comparable in magnitude to the sound frequency ω . This resonance condition is easily discernible from the denominator of Eq. (B-1) in Appendix B. Cyclotron resonances are not observable in our copper, silver, and gold specimens at the frequencies we use here because the purities of the samples are not great enough to satisfy the necessary condition $\omega\tau \geq 1$, where τ is the mean time between collisions.

Quantum oscillations are due to the quantization of the electron orbits in the magnetic field and appear in the factor Q in Eq. (B-1) in Appendix B. They occur when the energy level separation is greater than thermal broadening, i.e., when $\hbar\omega_c \geq kT$, where k is the Boltzmann constant and T the absolute temperature. We do not have high enough magnetic fields (> 27 kG) to observe quantum oscillations.

3. Open-Orbit Resonances

If the Fermi surface of a metal consists of multiply-connected surfaces in reciprocal space, and if a static magnetic field is applied to the metal in a certain direction perpendicular to the sound wave propagation direction, then some electrons may execute periodic open orbits. The electrons will absorb energy from the sound wave resonantly whenever the period of the open orbit D in real space matches the

sound wavelength, i.e., when

$$D = n\lambda, \quad n = 1, 2, 3, \dots \quad (2-4)$$

The portion of the attenuation coefficient due to open-orbit electrons can be obtained using the method of Pippard^{17,30}. This will be developed in the next chapter.

CHAPTER III

NUMERICAL CALCULATION OF OPEN-ORBIT RESONANCES

In this chapter we derive the expression for the attenuation of ultrasonic waves in metals due to electrons traveling on periodic open orbits. Our approach is essentially the same as that followed by Pippard^{17,30}. We will then reduce the expression to a form suitable for numerical calculations by making valid approximations. The method of numerical calculations will be developed. This will be based on the analytic expressions for the Fermi surfaces of the noble metals as developed by Halse⁴¹. An account of the computer program used to calculate the gradients for Halse's surfaces will also be outlined.

A. Theory

Suppose we have a transverse sound wave propagating in the direction of the open orbit in real space. This gives rise to transverse electric fields with the periodicity of the motion of ions. Assume $\omega\tau \ll 1$ so that we may treat the force fields as stationary with respect to the electron orbits. The force on the electron can be represented as $\vec{F}e^{iqx}$ ($\vec{q} \parallel x$ and x is along the open orbit direction). The force varies in a periodic manner along the orbit, always having the same value at corresponding points. As the electron

moves along its orbit, it acquires energy from the field at a rate given by

$$\frac{d\varepsilon}{dt} = \vec{F} \cdot \frac{d\vec{s}}{dt} e^{iqx} \quad , \quad (3-1)$$

if there are no collisions. By transforming coordinates, we have

$$\frac{d\varepsilon}{dx} = \vec{F} \cdot \frac{d\vec{s}}{dx} e^{iqx} \quad , \quad (3-2)$$

where s is distance measured along the actual path of the electron. If there are occasional collisions but ℓ is greater than the length of one cycle of the open orbit so that an electron can traverse many cycles of the orbit before being scattered, then the rate at which the electron absorbs energy from the field as it travels along the orbit from $-\infty$ is expressed as

$$\frac{d\varepsilon}{dx} = \vec{F} \cdot \frac{d\vec{s}}{dx} e^{(iq + 1/\ell)x} \quad , \quad (3-3)$$

When (3-3) is integrated from $-\infty$ to 0 we have the increment of energy $\Delta\varepsilon$ acquired from the field at $x=0$. Now, both \vec{F} and $\frac{d\vec{s}}{dx}$ are periodic functions having the periodicity of the open orbit. If the periodicity, projected along the x -axis, is D , we may expand $\vec{F} \cdot \frac{d\vec{s}}{dx}$ in a Fourier series:

$$\vec{F} \cdot \frac{d\vec{s}}{dx} = \sum_{n=-\infty}^{\infty} A_n e^{-2\pi i n x / D} \quad , \quad (3-4)$$

where $A_n = A_{-n}^*$. If we combine Eq. (3-4) with (3-3) and integrate over $-\infty \leq x \leq 0$, we arrive at an expression for the amplitude of $\Delta\varepsilon$:

$$|\Delta\varepsilon| = D \sum_{n=0}^{\infty} \frac{|A_n|}{[(D/\ell)^2 + (qD - 2\pi n)^2]^{1/2}}. \quad (3-5)$$

Correspondingly the attenuation coefficient α is given by¹⁷

$$\alpha = (4\pi^3 \hbar M v_s u^2)^{-1} \int (|\Delta\varepsilon|^2 / \ell) dA, \quad (3-6)$$

where M is the density of the metal, u is the particle velocity, and dA is an element of the Fermi surface. Using Eq. (3-5) in (3-6) and integrating, we arrive at

$$\alpha = \frac{D^2}{2\pi^2 \hbar^3 M v_s u^2 \ell} \sum_{n=0}^{\infty} \frac{|A_n|^2 m_c dk_z}{(D/\ell)^2 + (qD - 2\pi n)^2}, \quad (3-7)$$

where integrals of the form $\int dA$ have been reduced to²⁵

$$\int dA \Rightarrow \int d^2k \Rightarrow 2\pi \int (m_c / \hbar^2) dk_z,$$

where m_c is the cyclotron mass, dk_z is the electron wave-vector in the magnetic field direction, and v_s is the velocity of the sound wave. The coefficient A_n is obtained by taking the Fourier transform of Eq. (3-4):

$$A_n = (1/D) \int_0^D \vec{F} \cdot \frac{d\vec{s}}{dx} e^{2\pi i n x / D} dx. \quad (3-8)$$

Hence

$$A_n = (1/D) \int_0^{T_c} \vec{F} \cdot \vec{v} e^{2\pi i n x/D} dt, \quad (3-9)$$

where T_c is the cyclotron period and \vec{v} is the electron velocity. In \vec{k} -space, Eq. (3-9) can be expressed as

$$A_n = (1/P_0) \int_0^{P_0} \vec{F}(\vec{k}) \cdot \vec{v}(\vec{k}) e^{2\pi i n k_y/P_0} dk_y, \quad (3-10)$$

where P_0 is the period of the open orbit and k_y is the electron wavevector in the open-orbit direction.

From Eq. (3-7) we note that if the metal is very pure so that $D/\lambda \ll 1$, sharp maxima of the attenuation may be expected whenever $(2\pi n - qD)$ vanishes, i.e., whenever D is a multiple of the acoustic wavelength. The relative heights of the resonances are determined from the coefficients A_n given by Eq. (3-9). From the resonance condition:

$$qD = 2\pi n$$

$$\text{i.e.,} \quad D = n\lambda = \hbar P_0 / eB,$$

$$\text{it follows that} \quad P_0 = ev_s nB / \hbar c f \quad (3-11)$$

where f is the frequency of the sound wave. We can obtain the period of the open orbit from the field at which a resonance occurs.

Mertsching²⁶ expressed the portion of attenuation

due to a particular band of open orbits as

$$\Delta\alpha_L(\text{open}) \approx \frac{\omega^2}{2\pi^2 n^2 \rho_0 V_s^3} \sum_{n=-\infty}^{\infty} \frac{\left[\int \left(\frac{m}{\omega_c}\right) |\Lambda_n|^2 dk_z \right] \frac{1}{\omega_c \tau}}{\left(\frac{1}{\omega_c \tau}\right)^2 + n^2 \left[\frac{B_n}{B} - \left(1 + \frac{\omega}{n\omega_c}\right) \right]^2}, \quad (3-12)$$

where ρ_0 = density of the metal

$$\Lambda_n = \frac{1}{2\pi} \int_0^{2\pi} d\theta \Lambda_L(\theta) e^{-i\left\{\frac{1}{\omega_c} \int_0^\theta \vec{q} \cdot [\vec{v} - \vec{v}'] d\theta' + n\theta\right\}}$$

θ = orbital parameter giving the position of an electron along its trajectory in a given k_z plane ($\dot{\theta} = \omega_c$)

$$\vec{v} = \frac{1}{2\pi} \int_0^{2\pi} \vec{v} d\theta$$

$\Lambda_L(\theta) = \Lambda_L(\theta, k_z, E_f)$ is the longitudinal component of the deformation parameter, which is equivalent to that used by Pippard ($\Lambda = -\hbar v_K$). The resonance peaks are approximately Lorentzian in shape. The amplitudes are proportional to the fields at which the peaks occur and to the relaxation time of

the open orbit electrons:

$$\alpha_n \propto (\omega_c \tau) = q\ell \cos\psi/n, \quad (3-15)$$

where ψ is the angle between \vec{q} and the open orbit direction in real space. The relative resonance width at the half-amplitude point is found from Eq. (3-12) to be independent of n :

$$(\Delta B)_n/B_n = 2/n\omega_c \tau = 2/q\ell. \quad (3-16)$$

A series of resonances due to the "primary" band of open orbits running over successive "necks" of the Fermi surface of copper was first observed by Burmeister, Doan, and Gavenda³². Resonances associated with two "secondary" open orbit bands in copper have been reported by Kamm³³, and similar open orbits have been found in cadmium,³⁴ zinc,³⁴ tin,²¹ thallium,³⁶ rhenium,³⁷ and gallium.³⁸ More recently a Doppler-shifted secondary open-orbit resonance in copper

Doppler-shifted open-orbit resonances have also been reported in a crystal of gallium³⁸. Gavenda and Cox⁴⁰ have also reported the polarization dependence of the primary and secondary open-orbit resonances in copper. But prior to this investigation no such open orbit phenomena have been reported in silver or gold, and the relative heights of open-orbit resonances have not been determined by any model calculations.

B. Numerical Calculations

From Eq. (3-7) the attenuation coefficient due to open-orbit electrons can be expressed as

$$\alpha(\text{open}) \cong \frac{(D/\lambda)^2}{2\pi^2 n^3 M v_s^3 q^2 \ell} \sum_{n=0}^{\infty} \frac{\int |A_n|^2 m_c dk_z}{(D/\lambda)^2 (1/q\ell)^2 + (D/\lambda - n)^2}, \quad (3-20)$$

where we have used the identity $q = 2\pi/\lambda$. A_n is given by Eq. (3-9):

$$A_n = (1/nP_0) \int_{\text{period}} \vec{F} \cdot \vec{v} e^{2\pi i n k_y / P_0} dt, \quad (3-21)$$

where we have replaced x/D by k_y/P_0 .

There are various components of the force \vec{F} which can occur as indicated by Pippard¹⁷. These are:

- a) that due to deformation of the Fermi surface, $iqv_s \nabla \cdot \underline{K} \cdot \underline{\epsilon}$, in which \underline{K} is the deformation parameter which varies over the Fermi surface,
- b) that due to the relative velocity of the electron, $iqv_s \nabla k_Q$, and
- c) that due to the electric field, $e\vec{E} \cdot \vec{v}/v$.

In these expressions k_Q is the component of the electron wavevector along the propagation direction, $\underline{\epsilon}$ is the strain tensor and \vec{E} is the electric field set up by the sound wave. In general all these components of the force can occur but, by confining ourselves to propagation directions of high symmetry, we may avoid some of the potential complexities. In particular, for shear waves propagating along an axis of high symmetry, the second component of the force vanishes. The actual form of the deformation parameter \underline{K} is not well known and in this calculation we shall neglect the force due to it. With these assumptions the force boils down to the electric force, so the term $\vec{F} \cdot \vec{v}$ in Eq. (3-21) can be expressed as

$$\vec{F} \cdot \vec{v} \approx e\vec{E} \cdot \vec{v}. \quad (3-22)$$

In the actual calculation of A_n we have taken the effective force on the electron to be simply proportional and parallel to the ion displacement, and the velocity \vec{v} to be

proportional to the gradient of Halse's functions⁴¹ describing the Fermi surfaces of the three metals ($\vec{v}=1/\hbar(\nabla_{\vec{k}} E(\vec{k}))$). Halse's empirical expressions for the Fermi surfaces of the noble metals can be given as a Fourier expansion:

$$\begin{aligned}
 W_F = & 3 - \cos(Y/2)\cos(Z/2) - \cos(Z/2)\cos(Y/2) \\
 & - \cos(X/2)\cos(Y/2) \\
 & + C_{200} [3 - \cos(X) - \cos(Y) - \cos(Z)] \\
 & + C_{211} [3 - \cos(X)\cos(Y/2)\cos(Z/2) - \cos(Y) \\
 & \quad \cos(Z/2)\cos(X/2) - \cos(Z)\cos(X/2)\cos(Y/2)] \\
 & + C_{220} [3 - \cos(Y)\cos(Z) - \cos(Z)\cos(X) - \cos(X)\cos(Y)] \\
 & + C_{310} [6 - \cos(3X/2)\cos(Y/2) - \cos(3X/2)\cos(Z/2) \\
 & \quad - \cos(3Y/2)\cos(Z/2) - \cos(3Y/2)\cos(X/2) \\
 & \quad - \cos(3Z/2)\cos(X/2) - \cos(3Z/2)\cos(Y/2)], \quad (3-23)
 \end{aligned}$$

where $X = ak_x$, $Y = ak_y$, $Z = ak_z$, a is the lattice constant, k_x , k_y , and k_z are the components of the electron wavevector. Equation (3-23) results from an expansion of $E(\vec{k})$ in cubic harmonics. This form has been used earlier by Roaf⁴². The values of the constants used in the calculation are given as follows:

	W_F	C_{200}	C_{211}	C_{220}	C_{310}
Copper	1.69167	0.00693	-0.12668	-0.01679	-0.03772
Silver	-0.89789	-0.12030	-0.90187	-0.14086	-0.04483
Gold	-2.26213	-0.16635	-1.25516	-0.09914	-0.12704

These constants are so chosen so that the electron wavevectors on the Fermi surface deduced from the analytic expressions agree within 0.2% with the results of de Haas-van Alphen experiments. Halse's constants are an improvement over those obtained by Roaf⁴² with earlier data. The general appearance of the Fermi surfaces and the nomenclature for various extremal orbits (e.g., belly, neck, dog's bone, etc.) are also described by Shoenberg⁴⁵.

An orbit computer program developed by Wood⁴³ has been used to compute the gradients of Halse's functions for the copper, silver, and gold Fermi surfaces. The program accepts a given magnetic field (specified by its magnitude and two angular coordinates) and begins the calculation in the plane perpendicular to \vec{B} (through the center of the Brillouin zone unless otherwise specified). It steps around the orbit defined by the intersection of this plane with the Fermi surface (in the repeated zone scheme) until it returns to the original point or it decides that the orbit is open. As it goes around the orbit, it computes the components of the electron wavevector \vec{k} and the corresponding gradients of the surface at intervals specified by time dt in the expression

$$d\vec{k} = (e/\hbar c) (\nabla_{\vec{k}} E(\vec{k}) \times \vec{B}) dt.$$

An integration step size $dt = 10^{-6}$ has been used in computing $d\vec{k}$ and $\nabla_{\vec{k}} E(\vec{k})$. These are then used to compute A_n from Eq. (3-21).

The computed values of A_n are used in Eq. (3-20) to calculate the open orbit attenuation as a function of D/λ ($\sim 1/B$) and $q\ell$. The cyclotron mass m_c is proportional to the number of integration steps in one period which can be determined prior to the calculation of A_n . The integral over $m_c dk_z$ is achieved by dividing the open orbit band into suitable intervals of dk_z and carrying out the integration numerically using the trapezoidal rule. The periods of the primary and secondary open orbits in the noble metals were determined from the reciprocal lattice constants given by:

$$k_{[111]}a = 2\pi\sqrt{3}$$

and

$$k_{[010]}a = 4\pi,$$

where k is the Brillouin zone dimension in the open orbit direction and a is the lattice constant. Further details of the program Orbit are given in Appendix C.

CHAPTER IV

EXPERIMENTAL PROCEDURES

A. The Ultrasonic Technique

A block diagram of the apparatus used in the measurements is given in Fig. (4-1). Every 0.5 milliseconds a gated oscillator sends out two pulses: one is for sound excitation and the other is used to trigger the gate and the detector. The pulse for sound excitation is first amplified and then transmitted to a quartz transducer which is bonded to one face of the crystal sample by Nonaq stopcock grease or Dow Corning 200 fluid. The rf pulse, having been tuned to an odd multiple of the transducer fundamental frequency (10 MHz), is then converted into a sound wave packet which propagates back and forth through the metal until all its energy has been attenuated. The exponentially-decaying chain of ultrasonic pulses, picked up by the receiving transducer, is reconverted into electrical energy, amplified, and detected using a crystal detector. One of these pulses is gated and logarithmically converted to give a dc voltage level proportional to the total attenuation of the transmitted pulse in decibels. The change in this voltage level as a function of the magnetic field is assumed to give the relative

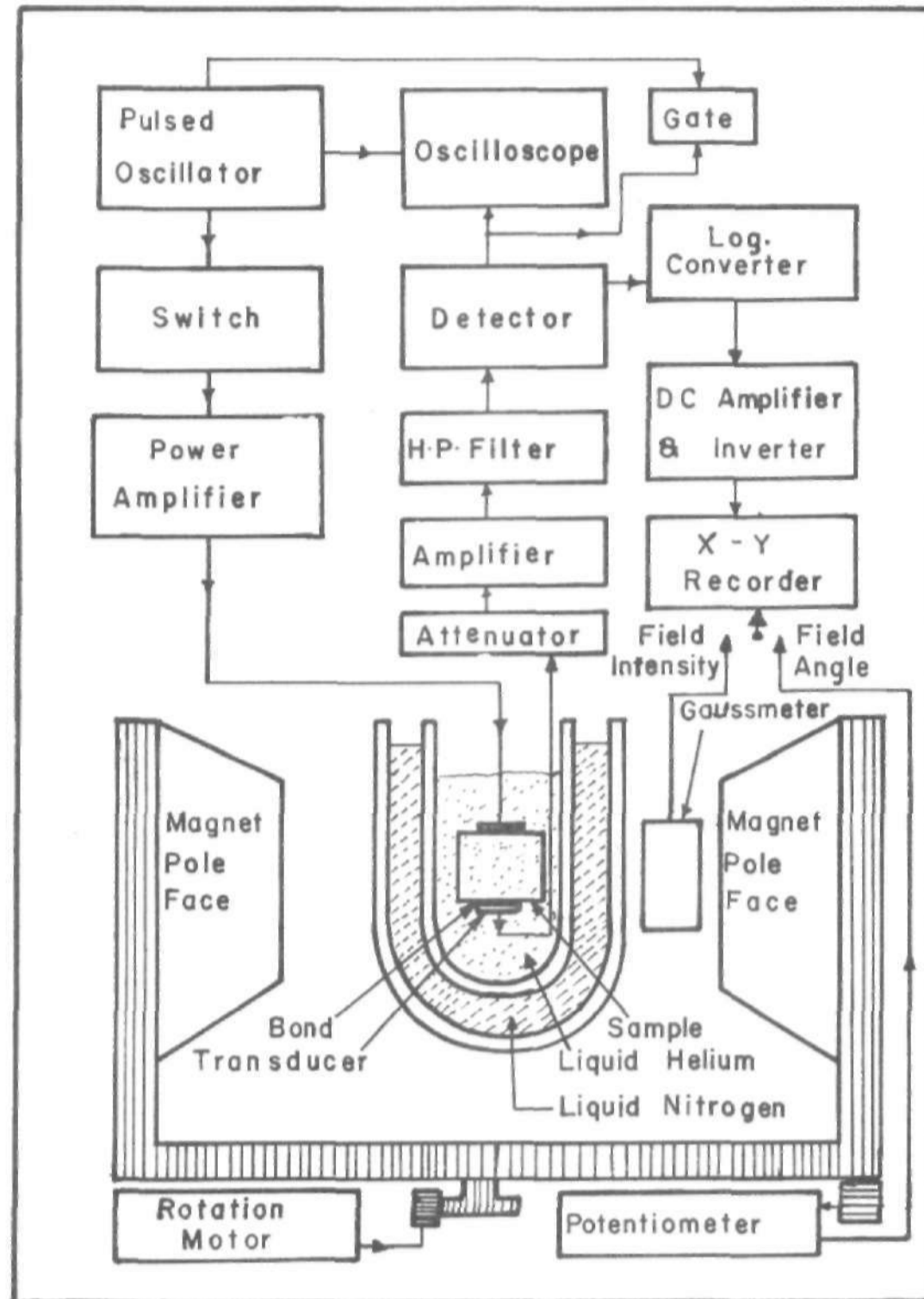


Fig. 4-1. Schematic diagram of experimental apparatus

attenuation $\alpha(B) - \alpha(0)$ due to the conduction electrons.

With a 15-inch Magnion electromagnet using a type FFC 3 field-control unit, field intensity sweeps could be made up to 27 kG with a stability and homogeneity of 5 parts in 10^5 . The field intensity is measured with a Rawson-Lush rotating-coil gaussmeter calibrated periodically with an NMR probe. The magnet turntable is motor-driven and coupled to a potentiometer which provides a voltage proportional to the relative angle of rotation of \vec{B} . In this way the relative attenuation can be recorded continuously as a function either of magnetic field intensity in a fixed position or of direction of \vec{B} in the rotation plane at a constant value of intensity. The recorded relative attenuation values are calibrated by inserting known amounts of attenuation in the receiver circuit. The frequency of the pulsed ultrasonic wave is determined by a frequency counter.

B. Sample Alignment in the Magnetic Field

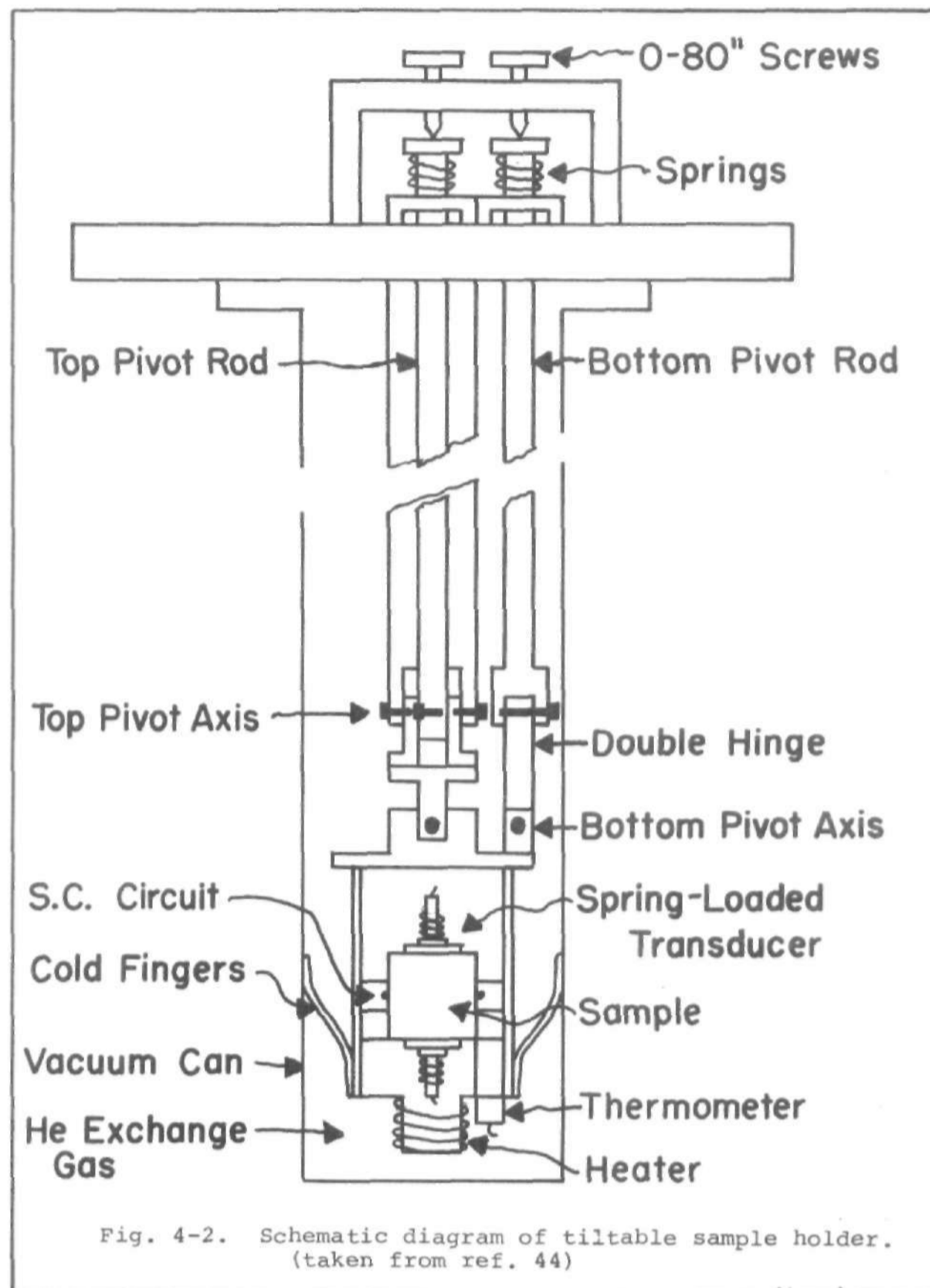
Because of the requirement that \vec{B} be perpendicular to the propagation direction ($\vec{B} \perp \vec{q}$) in order to observe open-orbit resonances, it is essential to have some means of orienting the samples with respect to the plane of rotation of \vec{B} . This is accomplished by means of a sample holder constructed by Cox⁴⁴. This is illustrated schematically in

Fig. (4-2). It enables the crystal to be tilted about two mutually-perpendicular axes in the rotational plane. The two tilt angles can be set to within 0.06° of any desired value over a $\pm 5^\circ$ range and, when combined with the rotation of the magnet in the horizontal plane, they provide the three degrees of freedom necessary for accurate alignment in the field.

The first task in each experimental run is to align the crystal sample so that the direction of propagation of the ultrasonic wave is perpendicular to the plane of rotation of \vec{B} . Two criteria are used for determining when the proper alignment has been achieved. First, a polar plot of the attenuation at low fields should reflect the symmetry of the Fermi surface about the direction of \vec{q} . Secondly, this polar plot should vary in a symmetric way when the crystal is tilted by positive and negative angles of equal magnitude away from the "on-axis" position. The alignment procedure then consists of taking polar plots at various tilt-angle settings until the symmetry indicates that \vec{q} is perpendicular to the plane of \vec{B} to within less than 0.1° .

C. Crystal Samples

The experimental data on copper which are used in this dissertation to test the validity of the calculated results were taken by Cox⁴⁰ on a single crystal of copper which



has a residual resistivity ratio ($\rho_{2730K}/\rho_{4.30K}$) of about 35,000. It has a length of 1.25 cm in the propagation direction ([101]).

The data on silver and gold were taken by the author on single crystals purchased with funds from the African-American Institute.* The silver has a length of 1.45 cm and the gold 0.2 cm in the propagation direction. The silver sample had an initial electron mean free path so short that magnetoacoustic oscillations could only be observed at frequencies above 110 MHz. In the gold sample, magnetoacoustic oscillations could only be seen at frequencies above 70 MHz. It was therefore necessary to oxidation-anneal⁴⁶ both samples in order to increase the electron mean free path so that the experiments could be performed at lower frequencies and fields.

The three samples were cut out of single crystals which were claimed to have initial chemical purities of 99.999%. The faces of the crystals were cut perpendicular to the corresponding symmetry axes to within 0.5° and were spark-planed flat and parallel to within 0.0001 inch.

D. Oxidation-Annealing

A block diagram of the oxidation-annealing process used is indicated in Fig. (4-3). The sample is thoroughly

* The silver and gold samples were purchased from the Department of Physics, Trinity University, San Antonio, Texas.

cleaned with distilled water and acetone and then etched with dilute nitric acid. It is then placed in a clean graphite boat which was previously heated at 850°C at a pressure of 4×10^{-5} T for twelve hours. The temperature of the sample is gradually raised to within 50°C of its melting point in four hours, keeping the pressure at 4×10^{-5} T. The sample is maintained under these conditions for five hours. Pure oxygen is then introduced and the pressure maintained at 4×10^{-4} T. The sample is cooked for forty-eight hours at this pressure of oxygen with the temperature maintained at 50 - 100°C below its melting point. (The silver was cooked at 820°C and the gold at 950°C .) The system is cooled down at a uniform rate not exceeding $50^{\circ}\text{C}/\text{hour}$ and at the working pressure. The temperature is monitored by a Chromel-Alumel thermocouple.

This oxidation-annealing increased the electron mean free path of the silver sample by a factor of about ten. Many magnetoacoustic oscillations could be seen in the silver at 31.7 MHz (see Fig. 4-4). The treatment had little effect on the gold sample although magnetoacoustic oscillations could be seen at 30 MHz after the annealing. The improvement in the electron mean free path brought about by this technique is thought to be due to some segregation of impurity oxides, in particular magnetic impurities, rather than any actual increase in chemical impurity. It should, therefore, be added

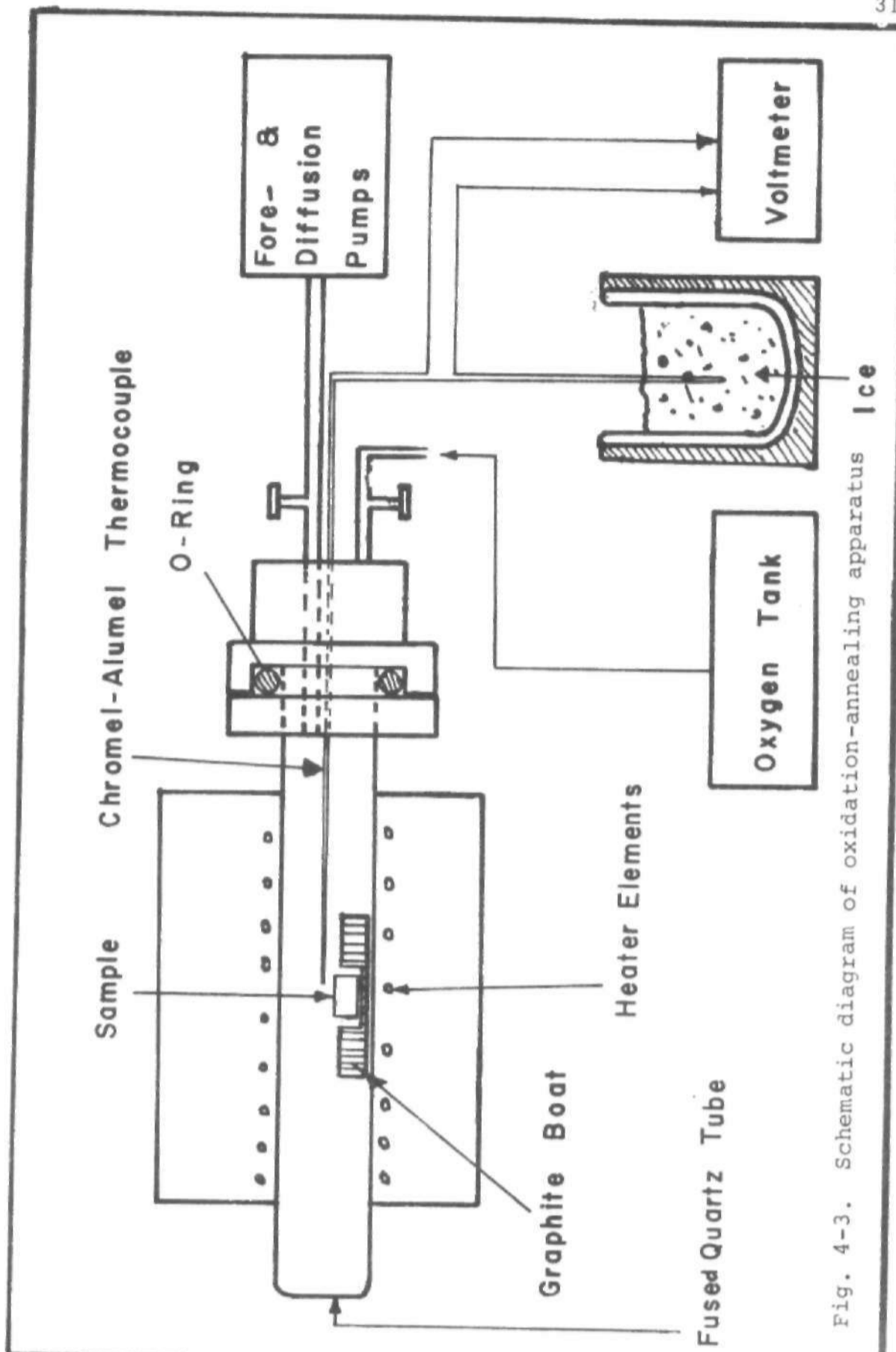


Fig. 4-3. Schematic diagram of oxidation-annealing apparatus

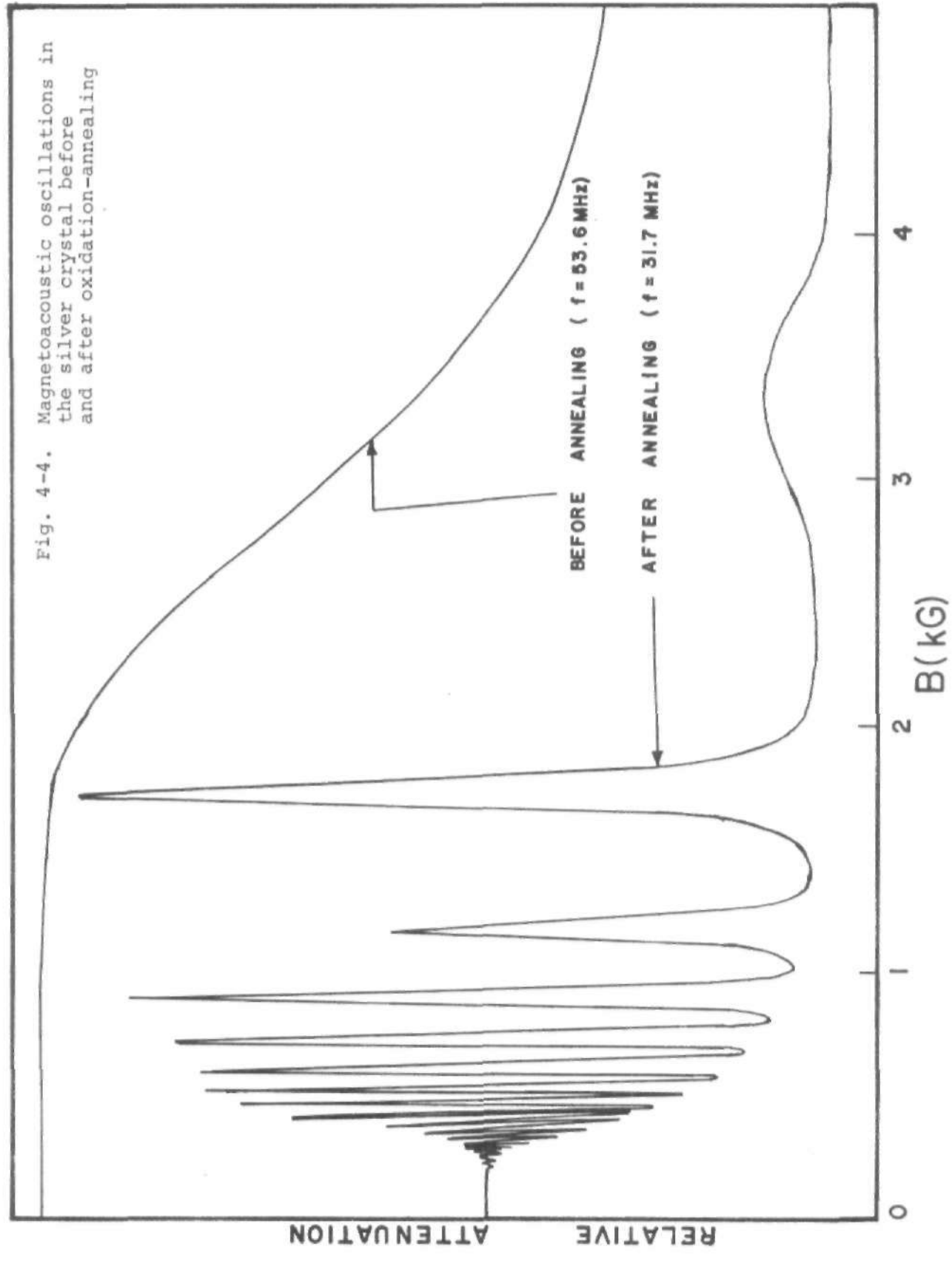


Fig. 4-4. Magnetoacoustic oscillations in the silver crystal before and after oxidation-annealing

that the term "purity" as used in this dissertation refers specifically to electron mean free path (as indicated by residual resistivity ratio) and not the relative concentration of chemical impurities. By comparison of the lowest fields at which oscillations occurred in the silver and gold with that in copper, their resistivity ratios after the annealing were estimated to be 15,000 and 2,000 respectively.

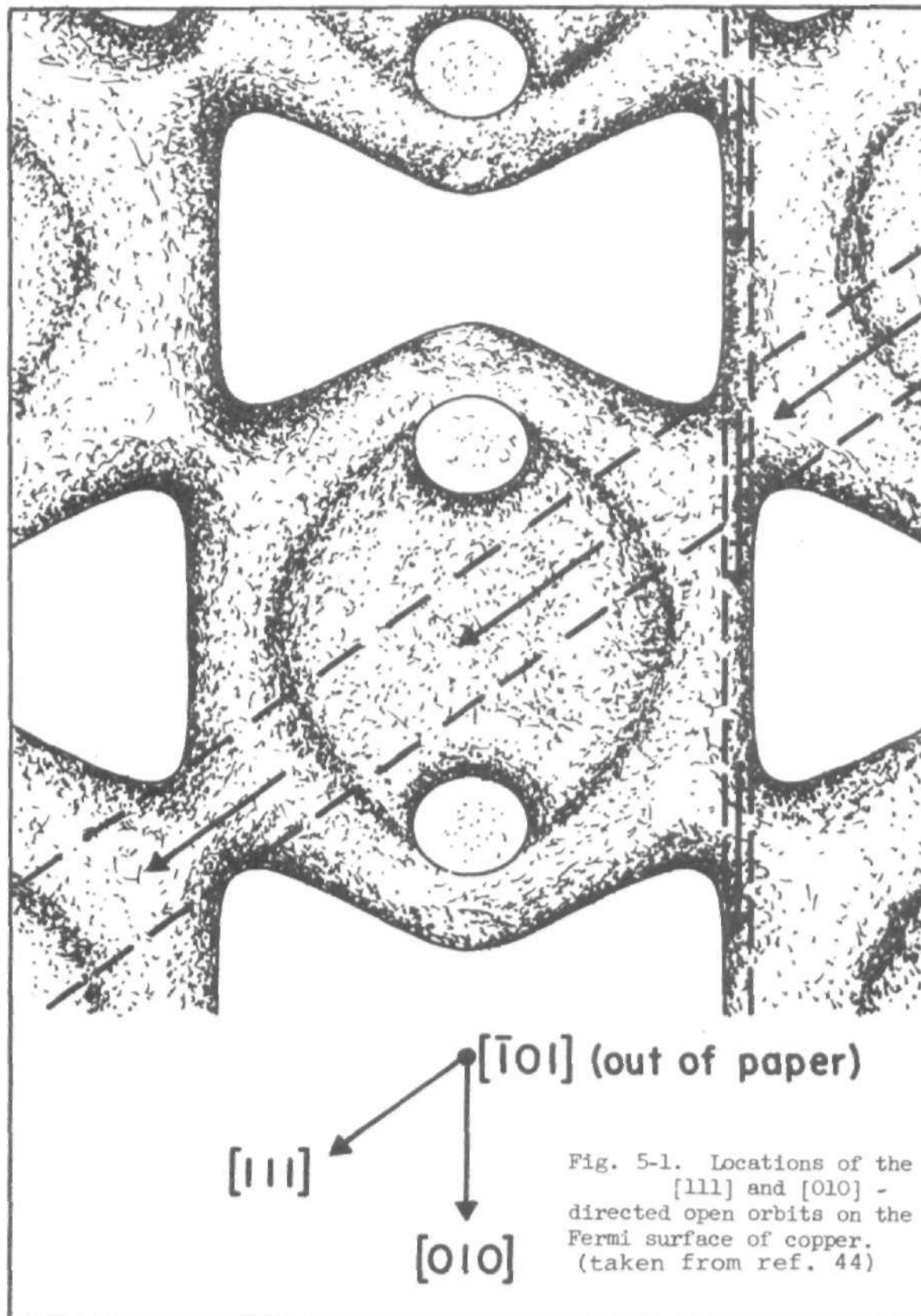
CHAPTER V

EXPERIMENTAL RESULTS

A. Introduction

The Fermi surfaces of the noble metals (copper, silver, and gold) are similar in general. In \vec{k} -space, they can be thought of as formed by pulling spheres out in the $[111]$ directions so that eight pointed regions (the necks) are formed. The regions make contact with the Brillouin zone boundaries. The sizes and shapes of the spheres and the necks differ from one noble metal to another. In general, therefore, we would expect the shapes of the resonant attenuation peaks in these metals to be similar, in particular the open-orbit resonances. We would, however, expect differences in the periods and strengths of the resonant absorption peaks.

Resonant absorption of ultrasound has been studied on two different bands of open orbits in the noble metals: the $[111]$ - and $[010]$ -directed open orbits. The locations of the $[111]$ and $[010]$ open orbit bands on the Fermi surface of copper are shown schematically in Fig. (5-1).



B. Copper Measurements

A detailed account of the measurements of ultrasonic attenuation by open-orbit electrons in copper has been reported by Cox and Gavenda^{29,40} using both compressional and shear waves propagating along $[\bar{1}01]$. The results of further analysis of the shear wave data will be given in the next chapter where we have plotted the attenuation α as a function of $1/B$ for the various magnetic field directions. This is necessary as it enables us to make direct comparison of the experimental results with the calculational results which we use to account for the various open orbit resonances.

C. Silver Measurements

1. Symmetry and Determination of Alignment

Before making measurements of the variations of relative attenuation with magnetic field \vec{B} , it was necessary to determine the exact orientation of the crystal axes of the sample when it was placed inside the cryogenic system. This was done by the conventional method involving a polar plot of the sound attenuation as a function of the direction of the magnetic field at a fixed value of the magnetic field (the value of the magnetic field used depends on the value that gives minute structure in the attenuation necessary to

determine the best alignment). The polar plot reflects the symmetry of the Fermi surface about the direction of \vec{q} . It should also vary in a symmetric way when the crystal is tilted by positive and negative angles of equal magnitude away from the "on-axis" position. Figure (5-2) shows an example of a polar plot taken on-axis with $\vec{B} \perp \vec{q}$ to within about 0.1° .

2. Compressional Waves Propagating Along $[\bar{1}01]$

The resonance peaks produced in silver by the $[111]$ -directed open-orbit band are shown in Fig. (5-3). These are obtained for $\vec{B} \parallel [1\bar{2}1]$. In addition to the fundamental resonance line, several subharmonic peaks can be seen (up to $n=8$) at $f = 52.8$ MHz superimposed on a weak series of geometric oscillations. For $\vec{B} \parallel [101]$ a weak resonance peak due to the $[010]$ -directed open orbit band was observed. This is shown in Fig. (5-4). No subharmonics were seen, the oscillations appearing at lower fields being geometric oscillations caused by electrons on extremal orbits of the lemon and dog's bone types. Cox and Gavenda²⁹ have seen such resonances in copper but Kamm³³ also reported two very weak $[010]$ subharmonics in copper in addition to the fundamental peak.

The periods of the open orbits have been calculated by using the values of the magnetic field at which the peaks occur in Eq. (3-11). In \vec{k} -space we find $P_{[111]} = 2.83 \pm 0.02 \times 10^{-19}$ g-cm/s and $P_{[010]} = 3.29 \pm 0.03 \times 10^{-19}$ g-cm/s. These

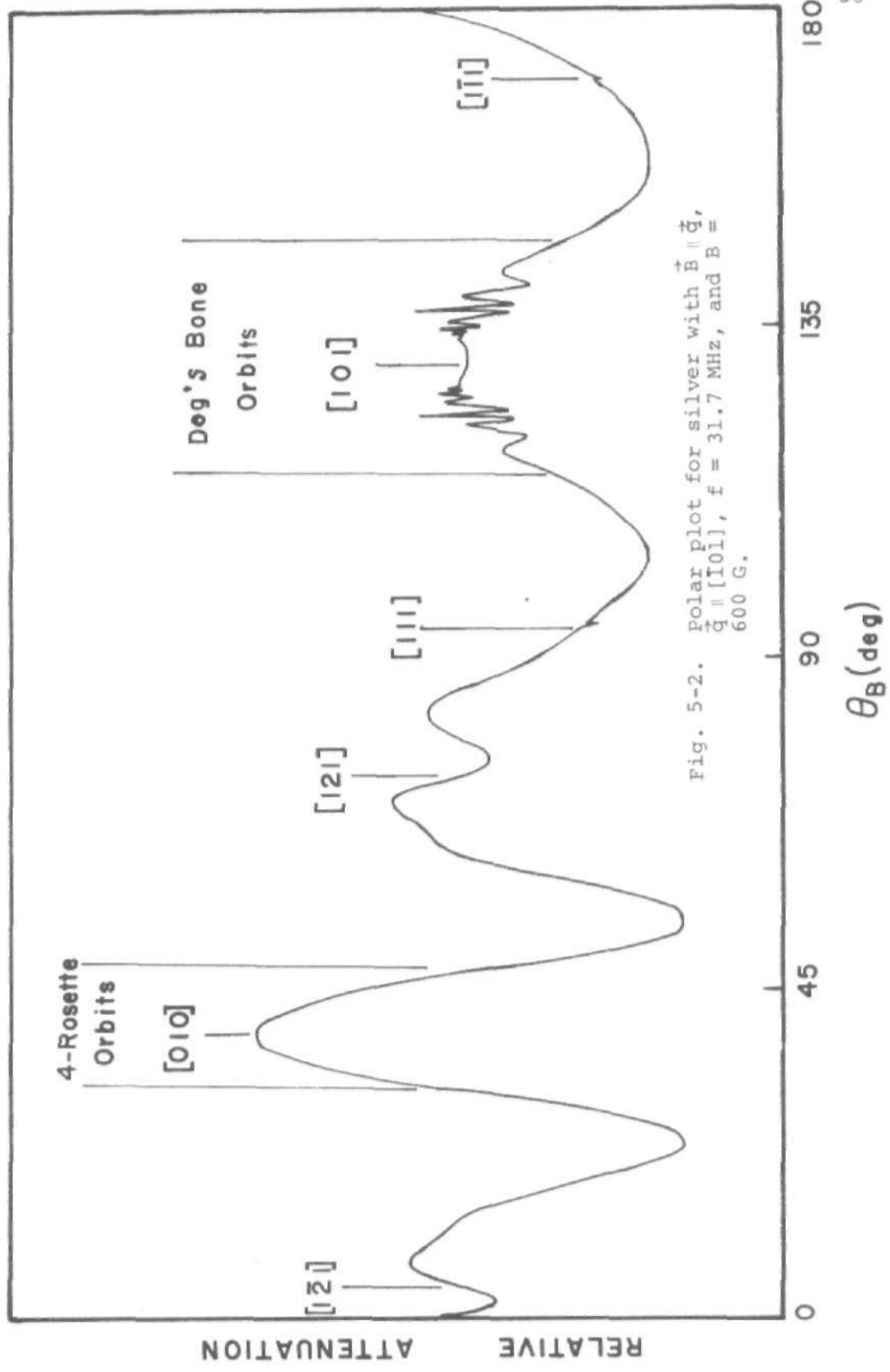


Fig. 5-2. Polar plot for silver with $\vec{B} \parallel \vec{q}$, $\vec{q} \parallel [101]$, $f = 31.7$ MHz, and $B = 600$ G.

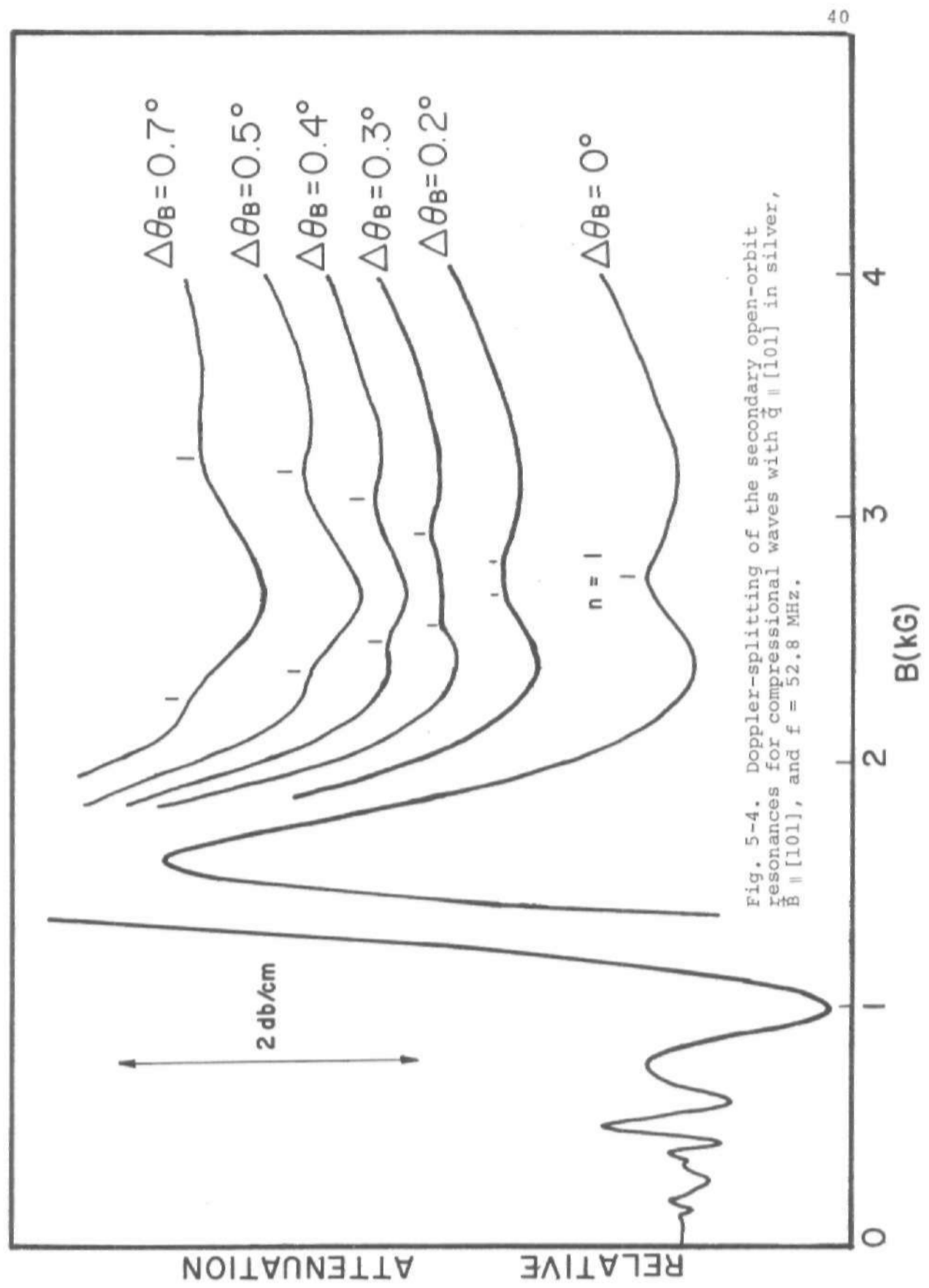


Fig. 5-4. Doppler-splitting of the secondary open-orbit resonances for compressional waves with $\vec{q} \parallel [101]$ in silver, $\vec{B} \parallel [101]$, and $f = 52.8$ MHz.

momenta are in good agreement with the values 2.82×10^{-19} g-cm/s and 3.40×10^{-19} g-cm/s for the [111] and [010] open orbits, respectively, calculated from the lattice constants. The resonance lines are approximately Lorentzian in shape and the electron mean free paths determined from the relative resonance width at half-amplitude points using Eq. (3-16) are (0.039 ± 0.005) cm and (0.014 ± 0.002) cm for the [111] and [010] open orbits respectively.

If \vec{B} is rotated slightly away from [101], the [010] open-orbit resonance splits into two Doppler-shifted peaks. The splitting widens rapidly with increasing $\Delta\theta_B$ and washes out completely when \vec{B} deviates from the symmetry axis by more than 1.0° (see Fig. (5-4)). The values of the open orbit period, the cyclotron mass, and the average velocity component along \vec{q} have been calculated using the observed resonance fields B_1^+ and B_1^- in Eqs. (3-17) to (3-19). The results are shown in Table (5-1). The period of the open orbit depends only on the Brillouin zone dimension along [010] and so is unaffected by rotation of \vec{B} away from [101]. However, the cyclotron mass increases very rapidly while the average velocity component along \vec{q} drops very rapidly as $\Delta\theta_B$ increases from 0.2° to 0.7° . It is this rapid reduction in \vec{v}_q due to alteration of orbit shape with field rotation (which does not take place for the [111] open orbit) that causes the Doppler-splitting of the [010] peak even though

$\omega\tau < 1$. When \vec{B} is exactly along the corresponding symmetry axes, m_c and v_q cannot be determined independently, but it is estimated from the program Orbit that electrons moving along the [010] open orbit have larger cyclotron masses (by a factor of 2.8) and smaller average velocity components (by a factor of 2.4) than the electrons on the [111] open orbit. We therefore expect shorter mean free paths for [010] open orbit electrons and correspondingly smaller attenuation peaks.

Table 5-1. Fermi velocity components and cyclotron mass calculated from Doppler-shifted data for the [010] open-orbit resonances in silver.

Angle of rotation away from in (101) plane (deg)	Open-orbit period ($\times 10^{-19}$ g-cm/s)	v_g/v_s	m_c/m_0
0.2	3.22	46.5	1.2
0.4	3.22	9.3	5.0
0.5	3.20	5.5	8.0
0.7	3.25	4.0	11.8

$v_s = 3.79 \times 10^5$ cm/s (compressional sound wave velocity)

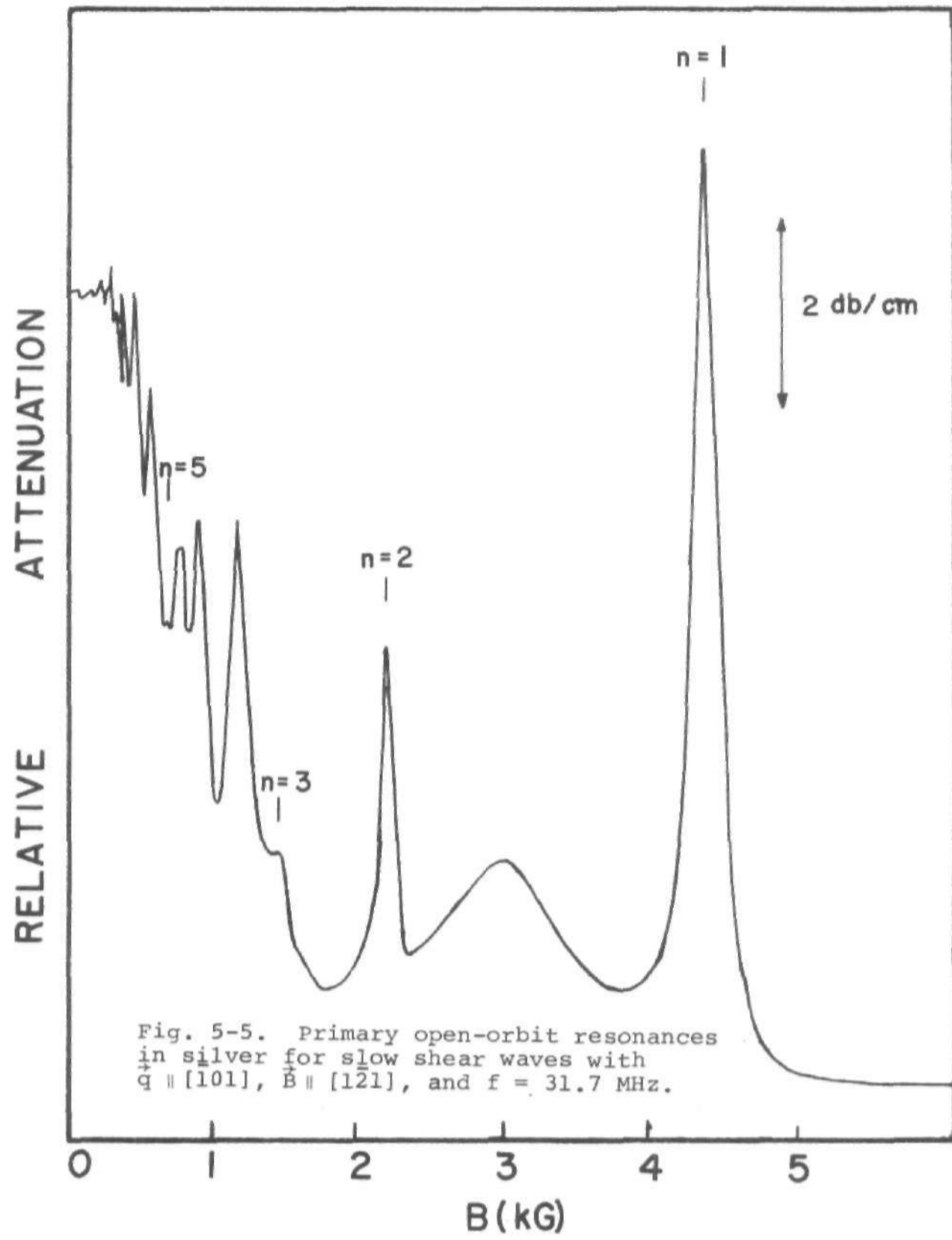
$m_0 = 9.11 \times 10^{-28}$ g (free electron mass)

3. Shear Wave Data

Measurements of attenuation of shear waves propagating along $[\bar{1}01]$ in silver were made with 30 and 50 MHz waves with two different polarizations. For a sound wave propagating along $[\bar{1}01]$, there are two shear modes: a slow mode with $\vec{\epsilon} \parallel [101]$ and a faster one with $\vec{\epsilon} \parallel [010]$. The field \vec{B} was rotated in the (101) plane so that it was always perpendicular to \vec{q} . When \vec{B} is along $[1\bar{2}1]$ to give the primary open orbit, it makes angles of 35.3° and 54.7° , respectively, with the polarization vectors of the slow and fast modes. When it is along $[101]$ to give the secondary open orbit, it is parallel to the slow mode polarization vector and perpendicular to the fast mode polarization vector.

a) Primary Open-Orbit Resonances

Figure (5-5) shows the primary open orbit resonance peaks for the slow mode in silver. A sharply-defined fundamental with harmonics up to $n=5$ are clearly discernible. The height of the second harmonic is about one-half of the fundamental, but subharmonics for $n>2$ wash out rapidly. The resonance peaks for the fast mode are shown in Fig. (5-6). It shows a structure similar to that of the slow mode except that the height of the fundamental is somewhat smaller for the fast mode, about 10.5 dB/cm as compared with 19.3 dB/cm for the slow mode. However, this result is not surprising



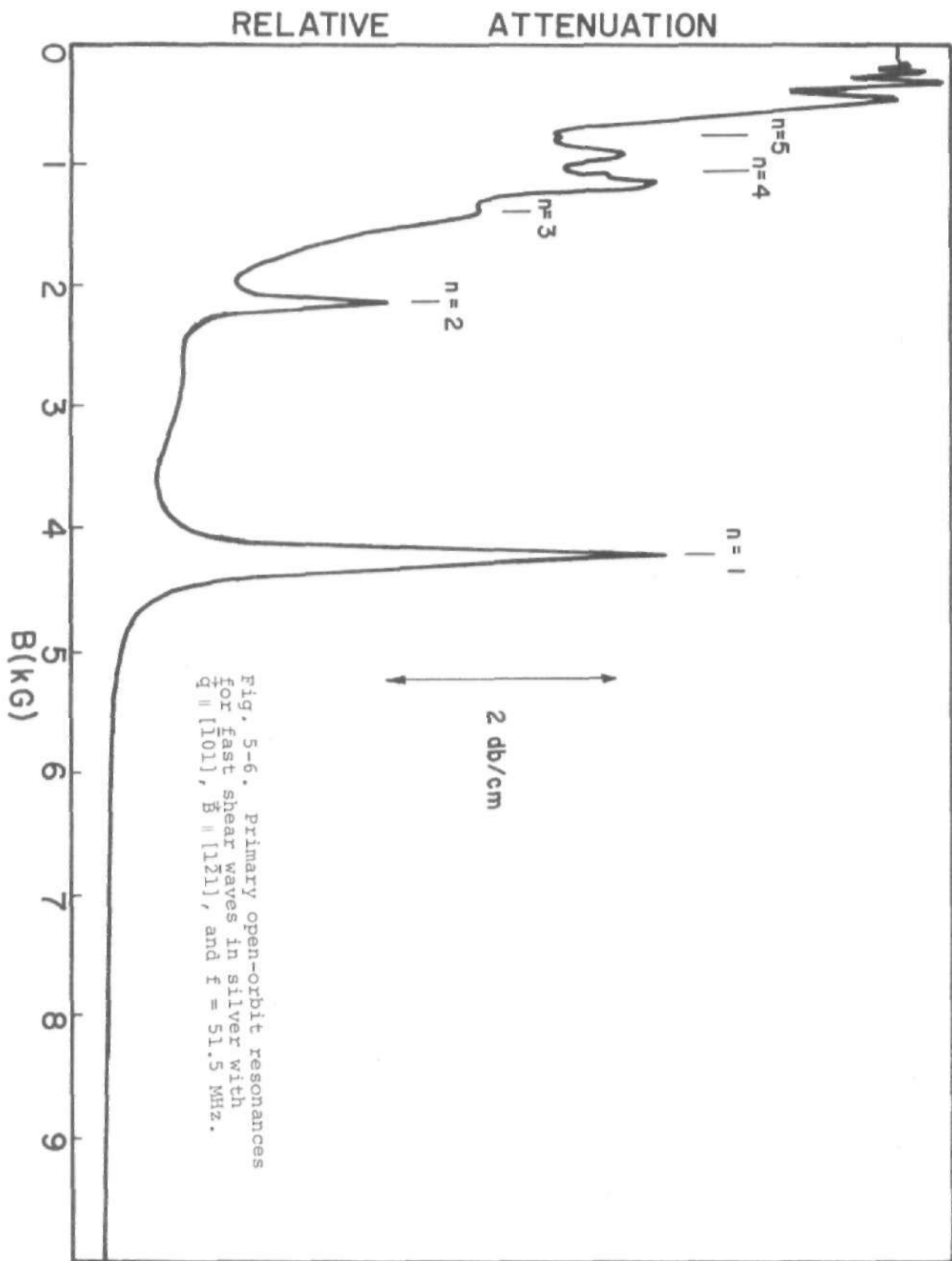


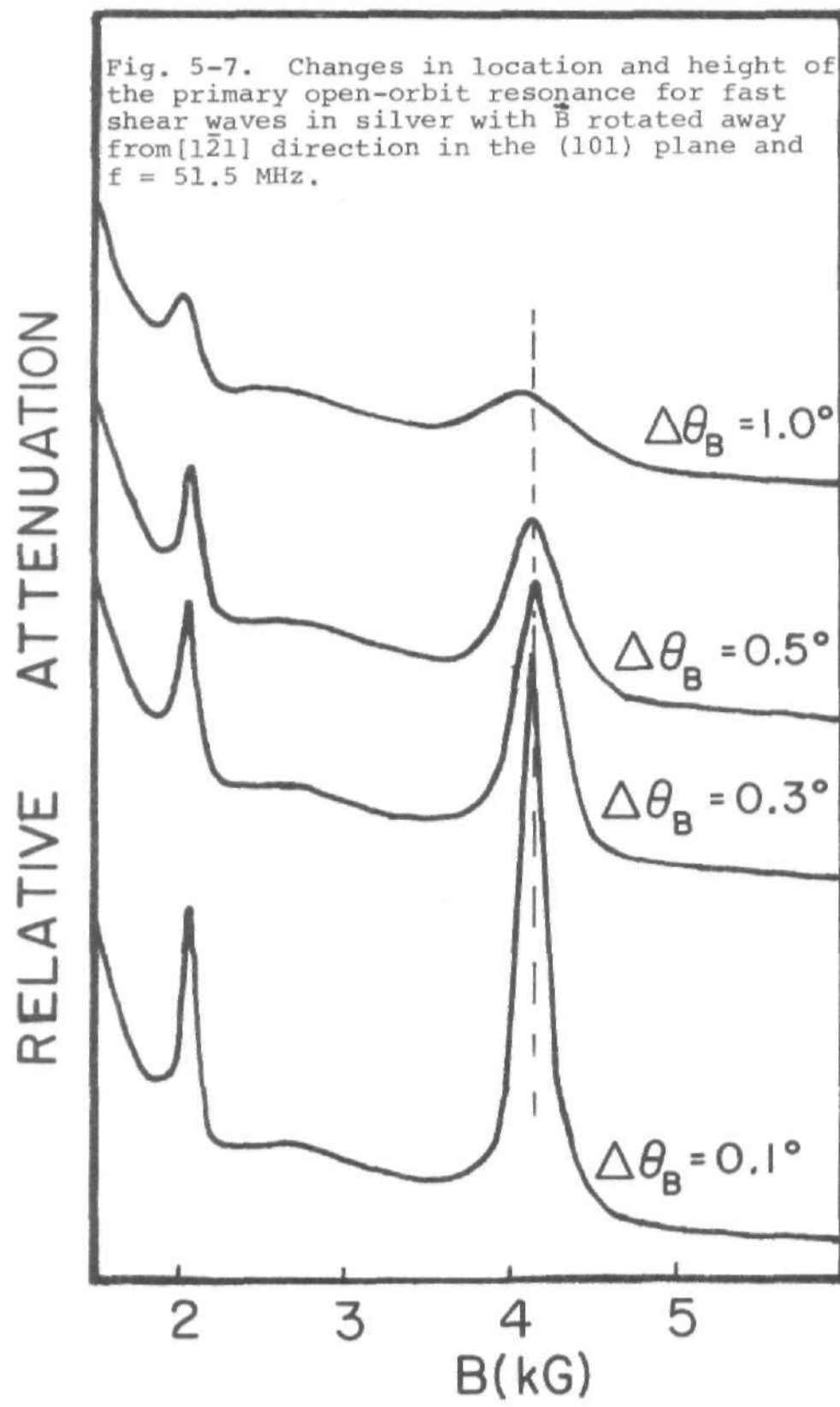
Fig. 5-6. Primary open-orbit resonances for fast shear waves in silver with $\vec{q} \parallel [101]$, $\vec{B} \parallel [1\bar{2}1]$, and $f = 51.5$ MHz.

as the attenuation is inversely proportional to the velocity of the sound waves and the fast mode has a velocity which is 1.96 times that of the slow mode in silver. The shape and location of the resonance changes with variation of the direction of \vec{B} from $[1\bar{2}1]$ in the (101) plane as illustrated in Fig. (5-7). The change in the location is negligible for $\Delta\theta_B < 1.0^\circ$. The periods of the open orbits as determined from the fields at resonances occur are consistent with those calculated from lattice constants. The electron mean free paths for the open orbits are also calculated from the relative resonance width at half-amplitude points and the results are tabulated in Table (5-2).

Table (5-2). Measured periods of open orbits and electron mean free paths from shear wave data in silver.

Open Orbit	Mode of Polarization	Open-Orbit period ($\times 10^{-19}$ g-cm/s)	ℓ (cm)
[111]	$\vec{E} \parallel [101]$	2.82	0.036
	$\vec{E} \parallel [010]$	2.82	0.037
	$\vec{E} \parallel [101]$	3.32	0.014
	$\vec{E} \parallel [010]$	--	--

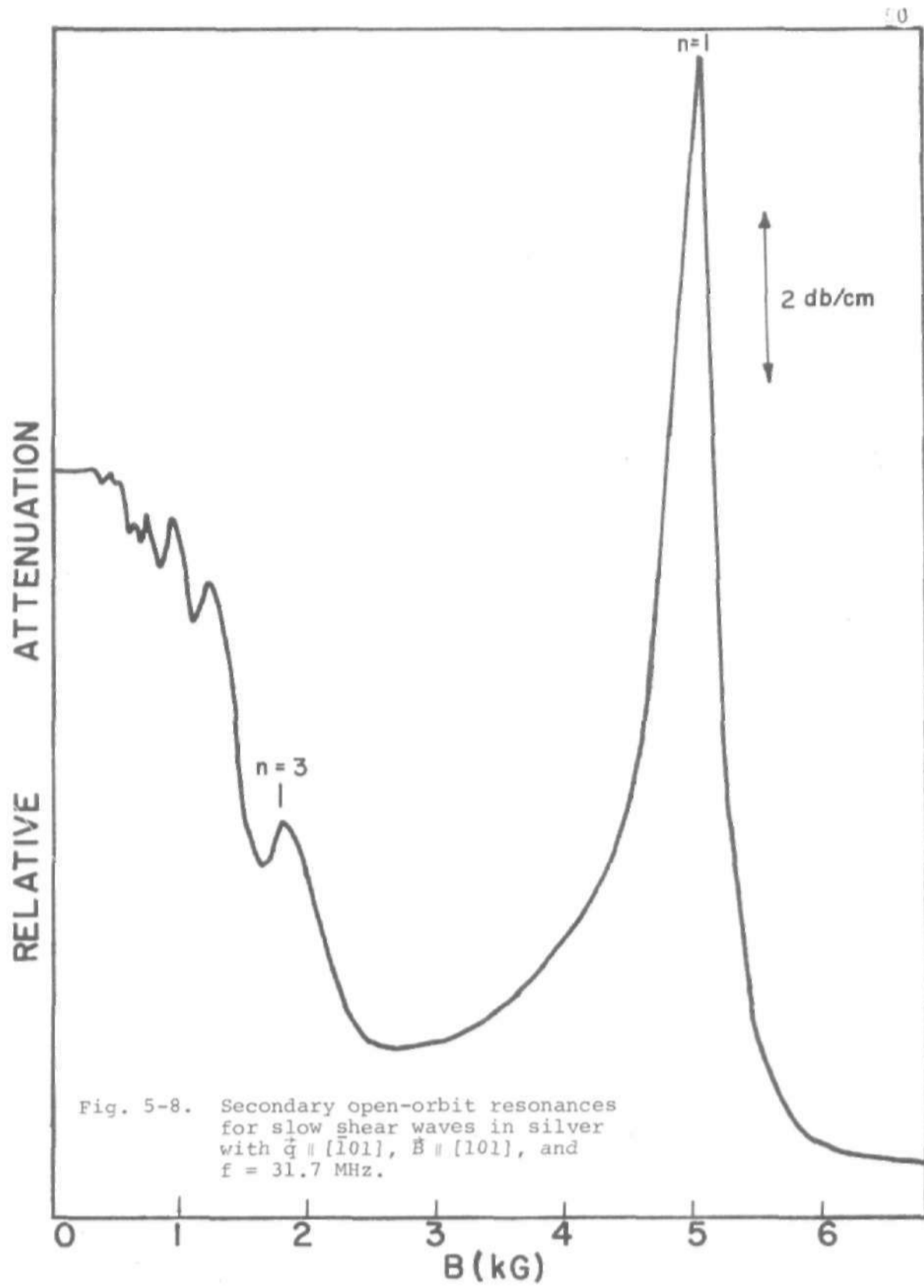
From lattice constants: $P_{[111]} = 2.82 \times 10^{-19}$ g-cm/s,
 $P_{[010]} = 3.40 \times 10^{-19}$ g-cm/s.



b) Secondary Open-Orbit Resonances

In Fig. (5-8) we show the resonance absorption peaks caused by electrons travelling along the [010] open orbit for shear waves with $\vec{\epsilon} \parallel [101]$. In this configuration, \vec{B} is parallel to the polarization vector. There is a strong fundamental resonance peak. A very weak third harmonic ($n=3$) is clearly evident but the $n=2$ harmonic is absent. A second harmonic weaker than the third was seen in copper by Cox and Gavenda⁴⁰ for the same configuration. Harmonics higher than $n=3$ were not seen, probably because they were obscured by geometric resonances at lower fields. Fig. (5-9) shows the rapid change in position and strength of the fundamental as \vec{B} is rotated away from [101].

Figure (5-10) shows the results for the fast mode, i.e., $\vec{\epsilon} \parallel [010]$. In this case $\vec{\epsilon}$ is perpendicular to \vec{B} . The fundamental resonance is not seen and only a small bump is observed at the field corresponding to the second harmonic. All other harmonics are absent. This is clearly contradictory to the usual interpretations of the free electron theories (CHH¹⁶) which predict that larger resonances occur for $\vec{\epsilon} \perp \vec{B}$. These surprising results are, however, explainable from the results of Fourier analysis of conduction electron velocities by ultrasonic shear waves to be discussed in the next chapter.

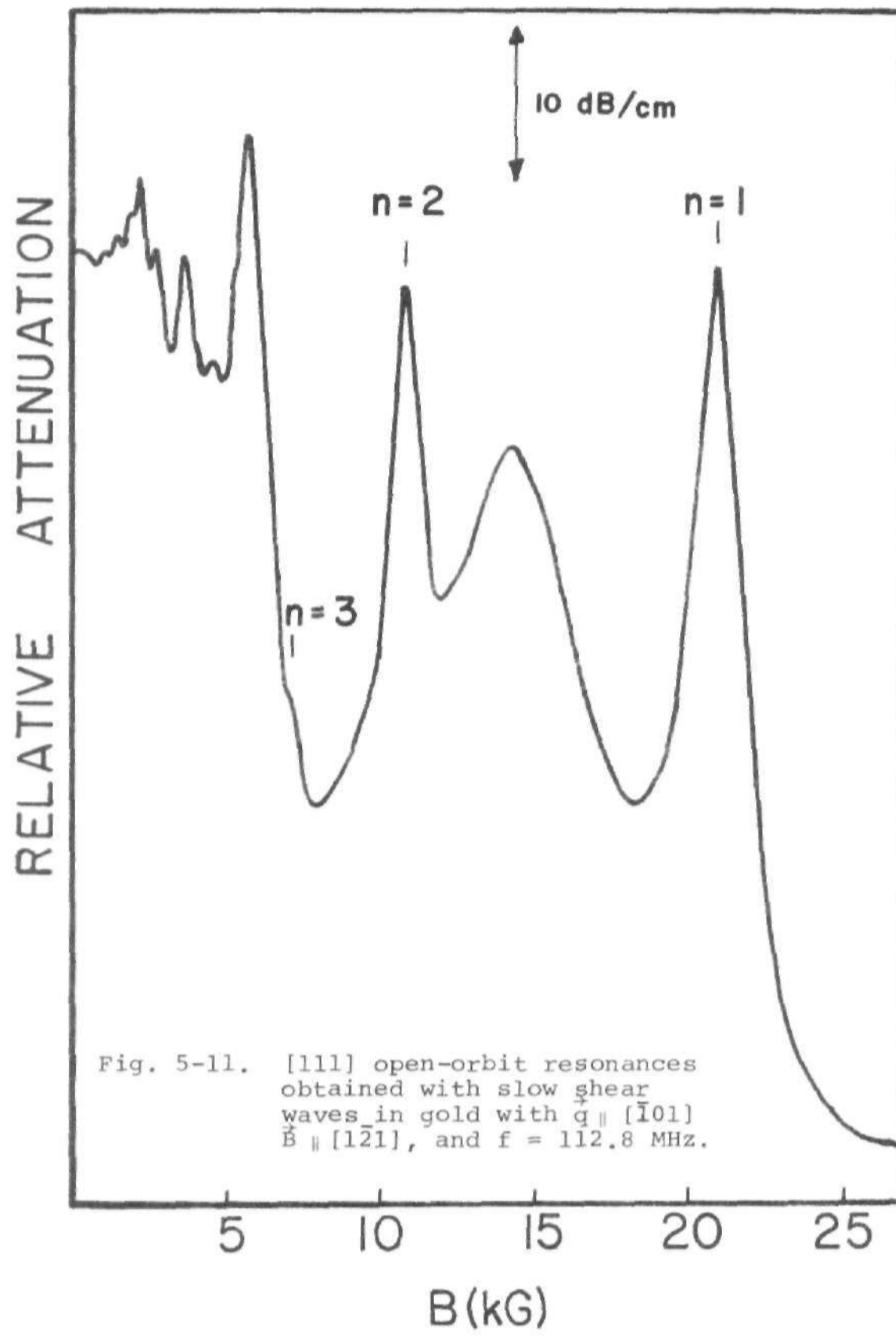


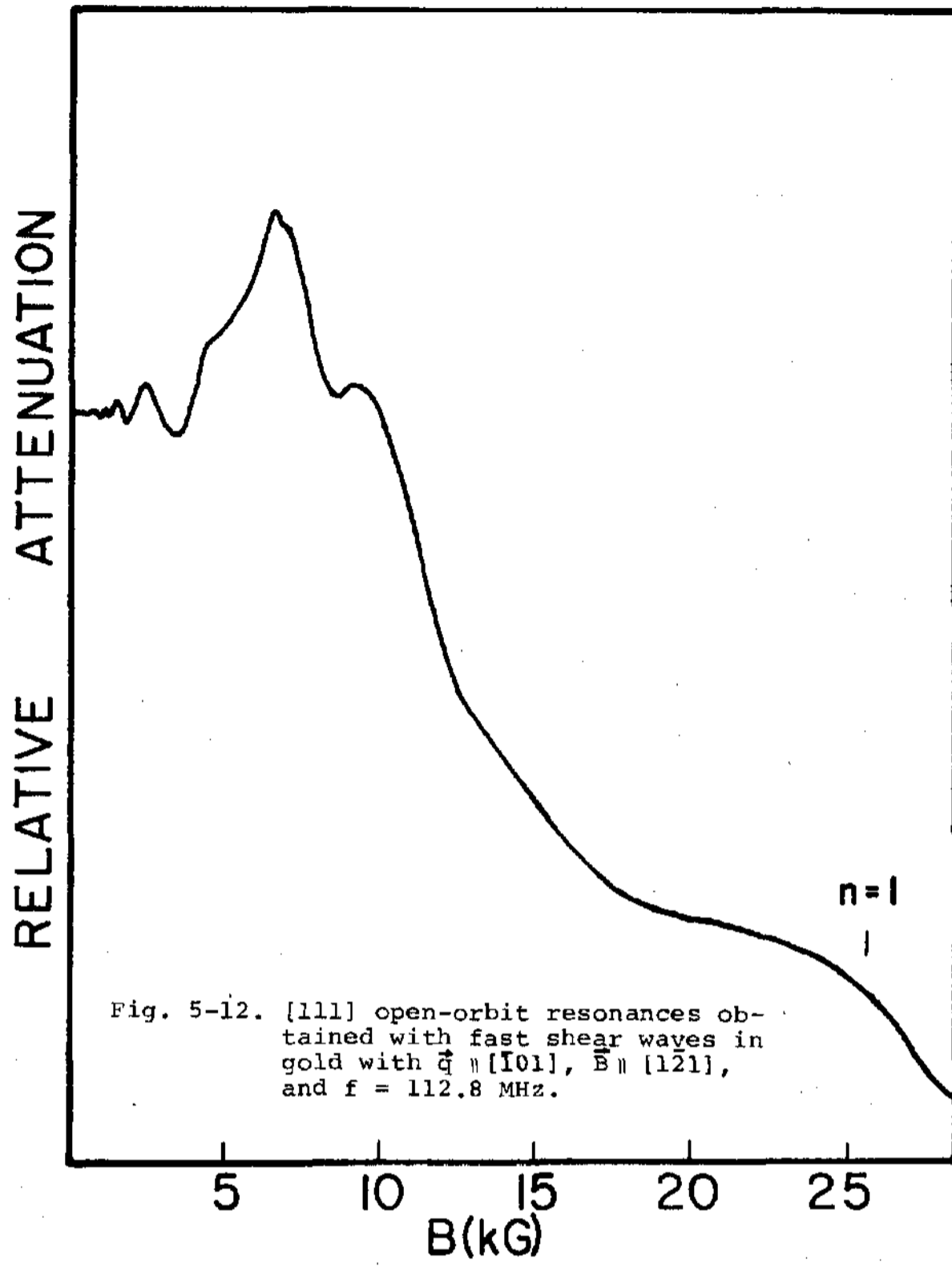
B(kG)

D. Gold Measurements

A limited amount of data were taken with gold using shear waves propagating along $[\bar{1}01]$ with polarization vector in the $[101]$ direction. The results with $\vec{B} \parallel [1\bar{2}1]$ are shown in Fig. (5-11). These primary open orbit resonances are similar to those observed in both copper and silver for the same configuration. The second harmonic compared with the fundamental is slightly stronger than observed in silver and copper. The purity of the gold sample is less than that of the copper and the silver so that we had to take measurements at a frequency of 110 MHz to observe peaks comparable with those seen in copper and silver. The results with $\vec{B} \parallel [101]$ are shown in Fig. (5-12). A small bump is seen where the fundamental is expected. The failure to observe the resonance peaks in this case is probably due to the low qz (about 5) value or improper sample alignment so that \vec{B} was not exactly perpendicular to \vec{q} , a condition very essential for the observation of the resonances.

The period of the $[111]$ open orbit calculated from the field where the fundamental resonance occurred is $2.62 \pm 0.03 \times 10^{-19}$ g-cm/s (compare with the value 2.66×10^{-19} g-cm/s calculated from lattice constants). The electron mean free path determined from the resonance line is (0.0026 ± 0.0004) cm.





CHAPTER VI

DISCUSSION AND INTERPRETATION OF RESULTS

A. Shear Wave Results

The general features of the experimental results can be explained by considering the motion of the electrons along the magnetic field \vec{B} as well as in the plane perpendicular to \vec{B} as outlined by Gavenda and Cox⁴⁰. These displacements, referred to as S_{\parallel} and S_{\perp} , are calculated from the program Orbit described in detail in Chapter III. S_{\perp} can be obtained by constructing cross-sections of the Fermi surface in planes perpendicular to \vec{B} , scaling dimensions by $\hbar c/eB$, and rotating the resulting curve by 90° . S_{\parallel} is obtained by integrating $v_{\vec{B}}$, the component of the Fermi velocity along \vec{B} , with respect to time.

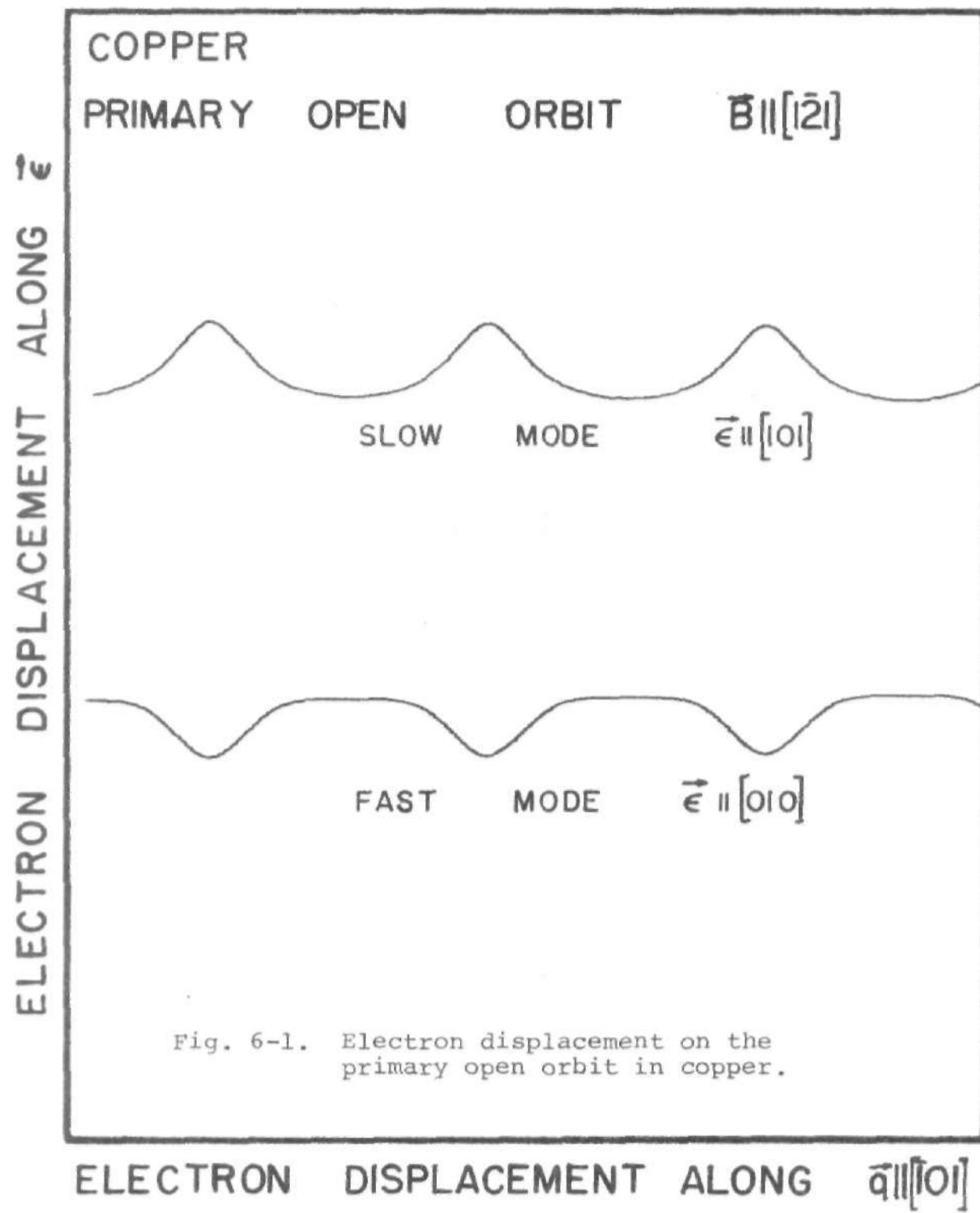
For sound waves propagating along $[\bar{1}01]$, we have calculated the electron displacements parallel to $\vec{E}_{\parallel}[101]$ and $\vec{E}_{\parallel}[010]$, respectively, for both primary ($\vec{B}_{\parallel}[1\bar{2}1]$) and secondary ($\vec{B}_{\parallel}[101]$) open orbits. Note that, for $B_{\parallel}[1\bar{2}1]$, S_{101} and S_{010} each involve both S_{\parallel} and S_{\perp} . Figures (6-1) through (6-3) show the resulting S_{101} and S_{010} as functions of position along the direction of propagation for the primary open orbits, whereas Figs. (6-4) through (6-6) show the

corresponding results for the secondary open orbits for the three metals.

The general patterns of the displacement are similar for the noble metals except for the differences in periods and amplitudes. These results are not surprising since their Fermi surfaces are similar except for the differences in sizes of the Fermi spheres and the necks as mentioned in the previous chapter.

For the primary open orbit, Figs. (6-1)-(6-3) show that the displacements along each polarization direction have approximately equal amplitudes, so one might expect the heights of the resonances to be equal. However, as mentioned in the previous chapter, the differences in the sound velocities for the two different polarization directions account for the differences in the resonant heights. The displacements also contain higher harmonics, accounting for the strong subharmonics in the attenuation resonant peaks seen in the experiment.

For the secondary open orbit, the displacement parallel to \vec{B} is much larger than that perpendicular to \vec{B} (see Figs. (6-4) to (6-6)). In addition, the period of the oscillation in S_{010} is one-half that of S_{101} . Also, only the fundamentals are apparent in the displacements. These factors account for the experimental results on the [010] open orbit: for $\vec{E} \parallel [101]$, ($\vec{E} \parallel \vec{B}$), a large fundamental is seen (Fig.(5-8),



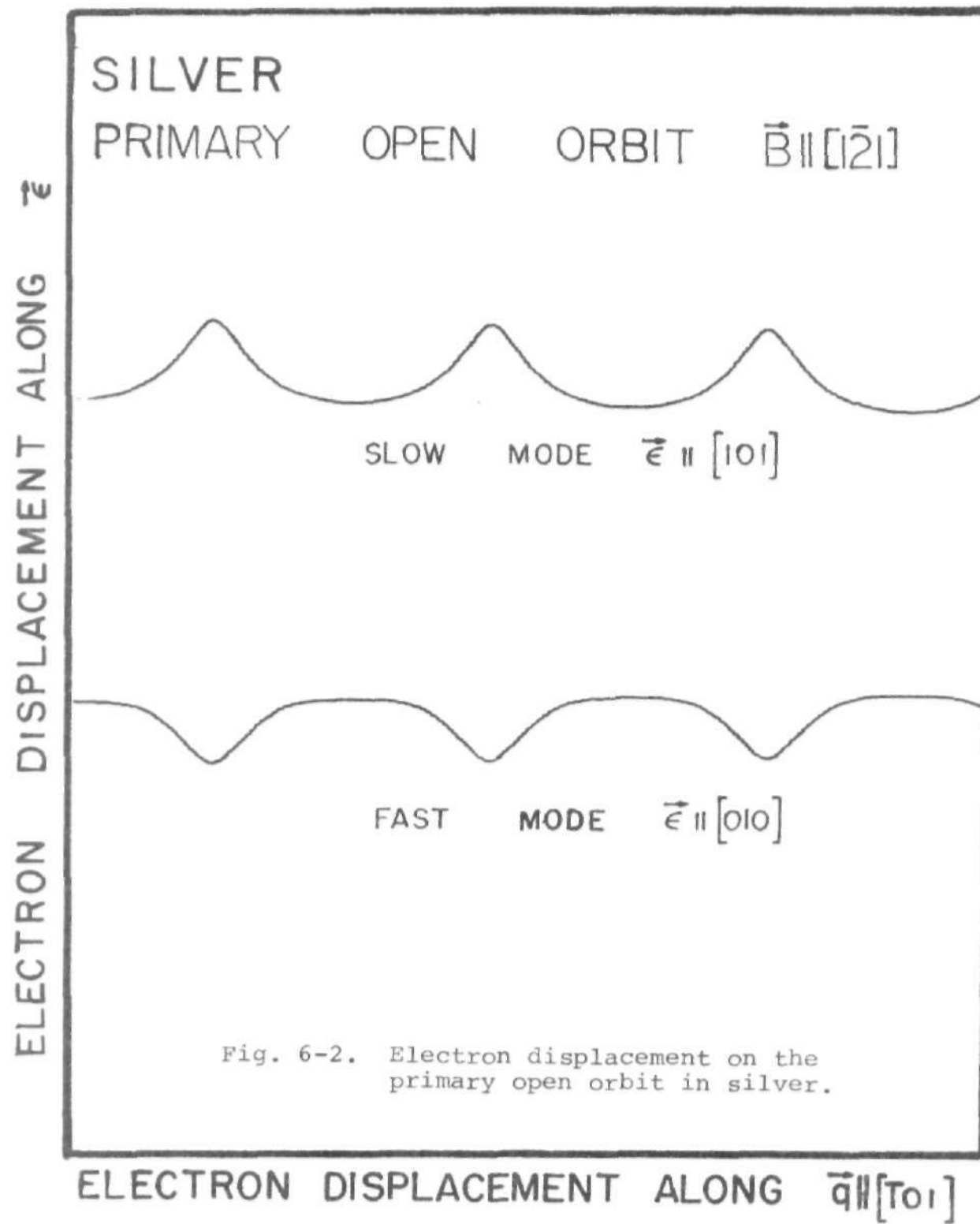
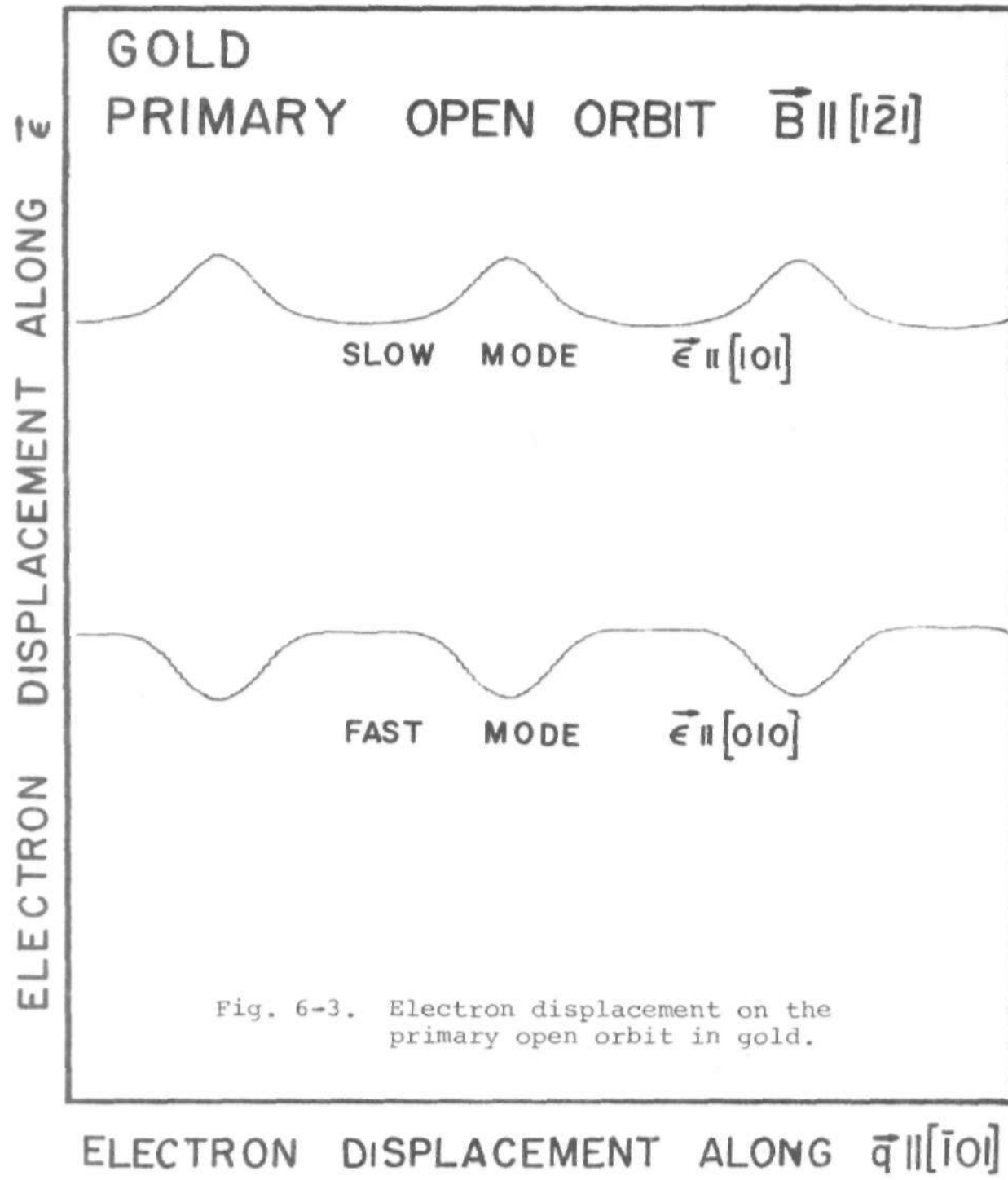
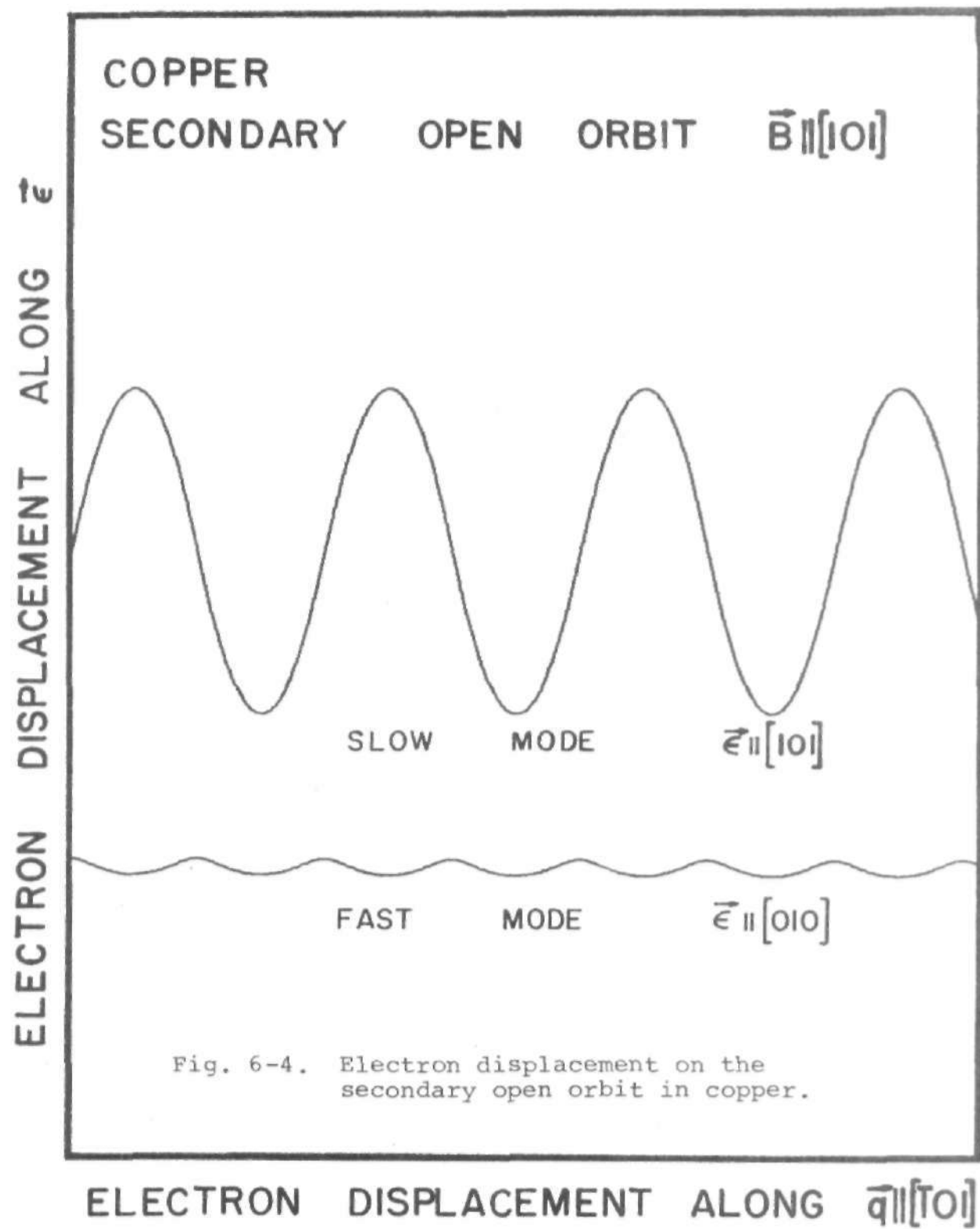


Fig. 6-2. Electron displacement on the primary open orbit in silver.





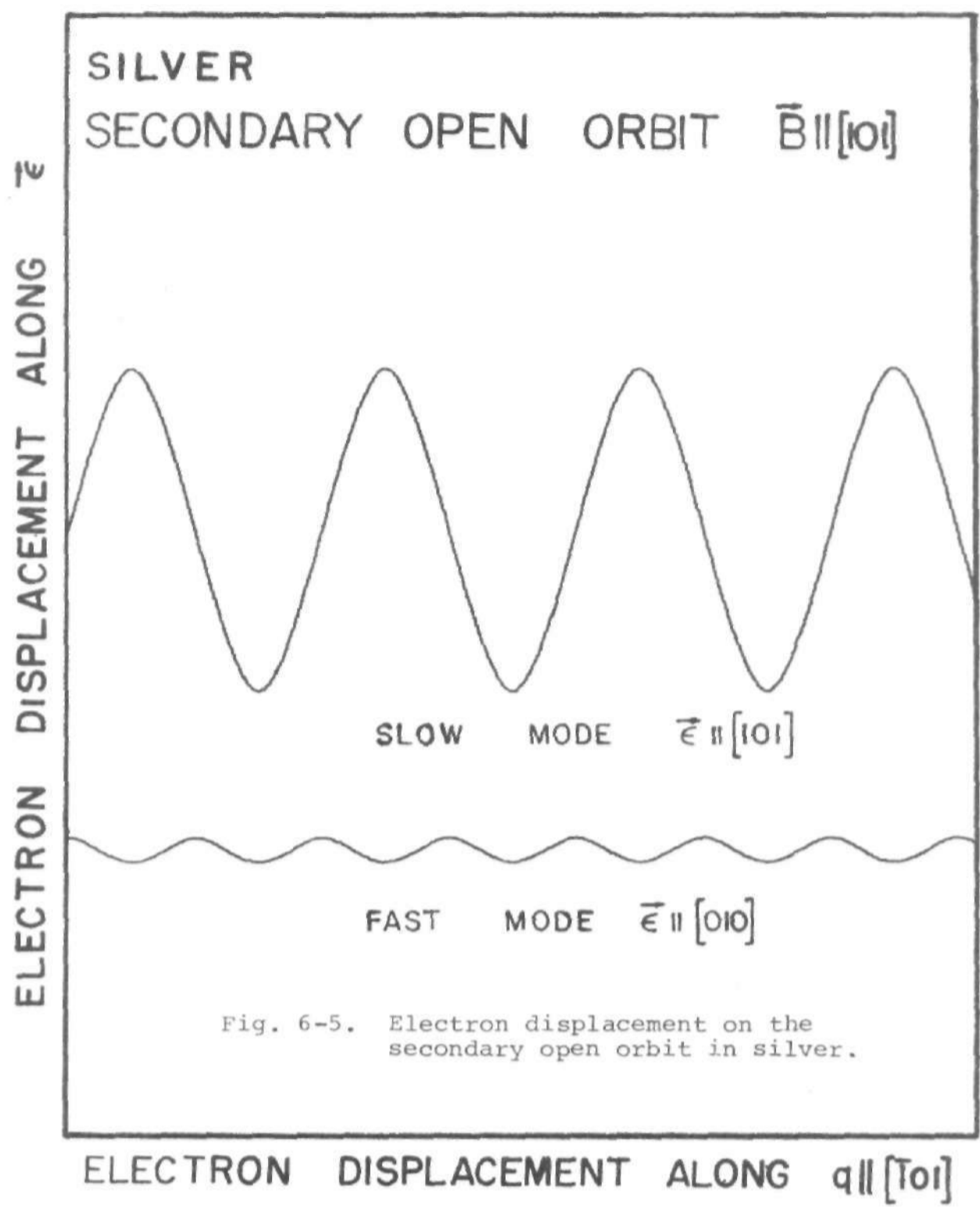


Fig. 6-5. Electron displacement on the secondary open orbit in silver.

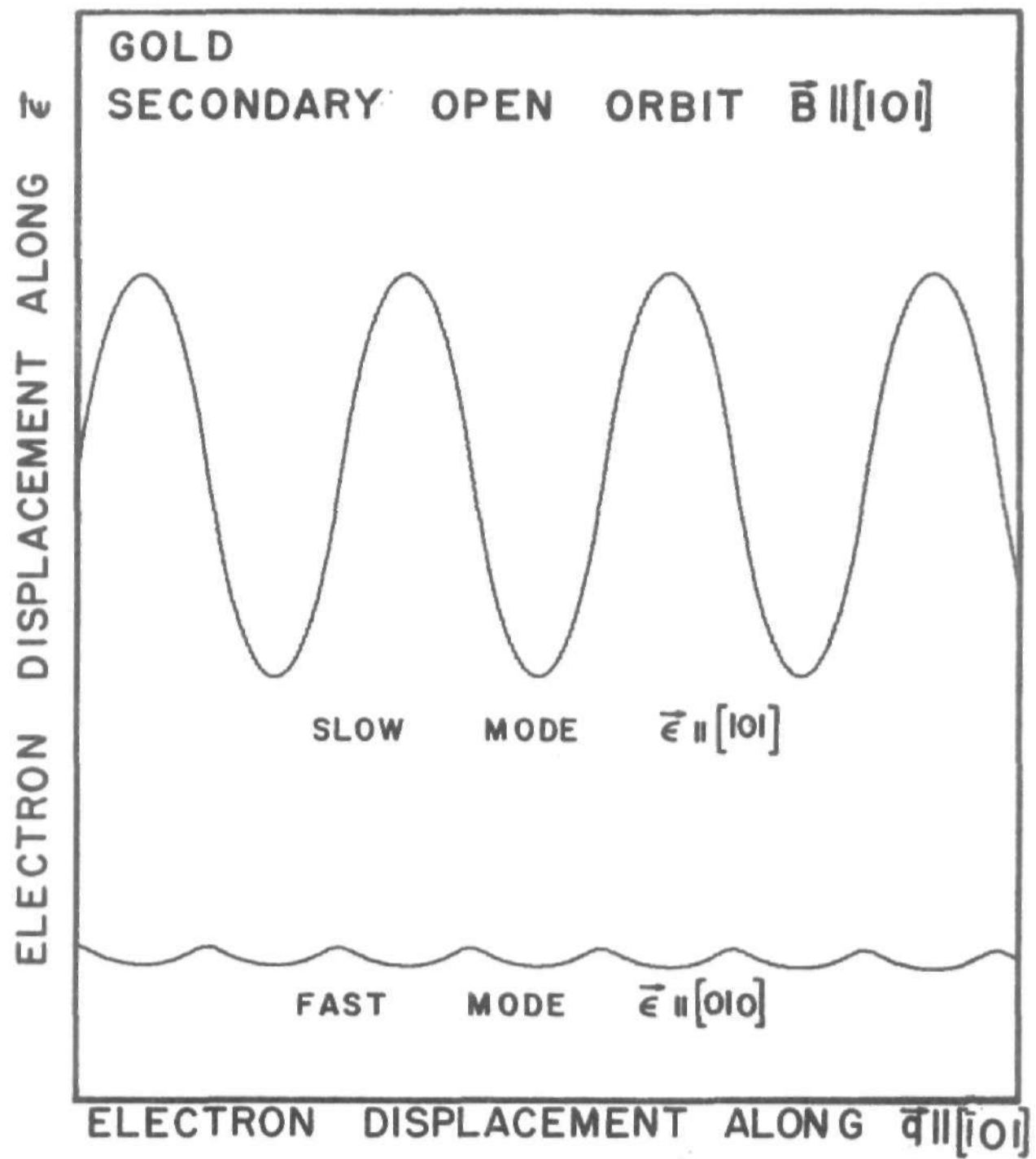
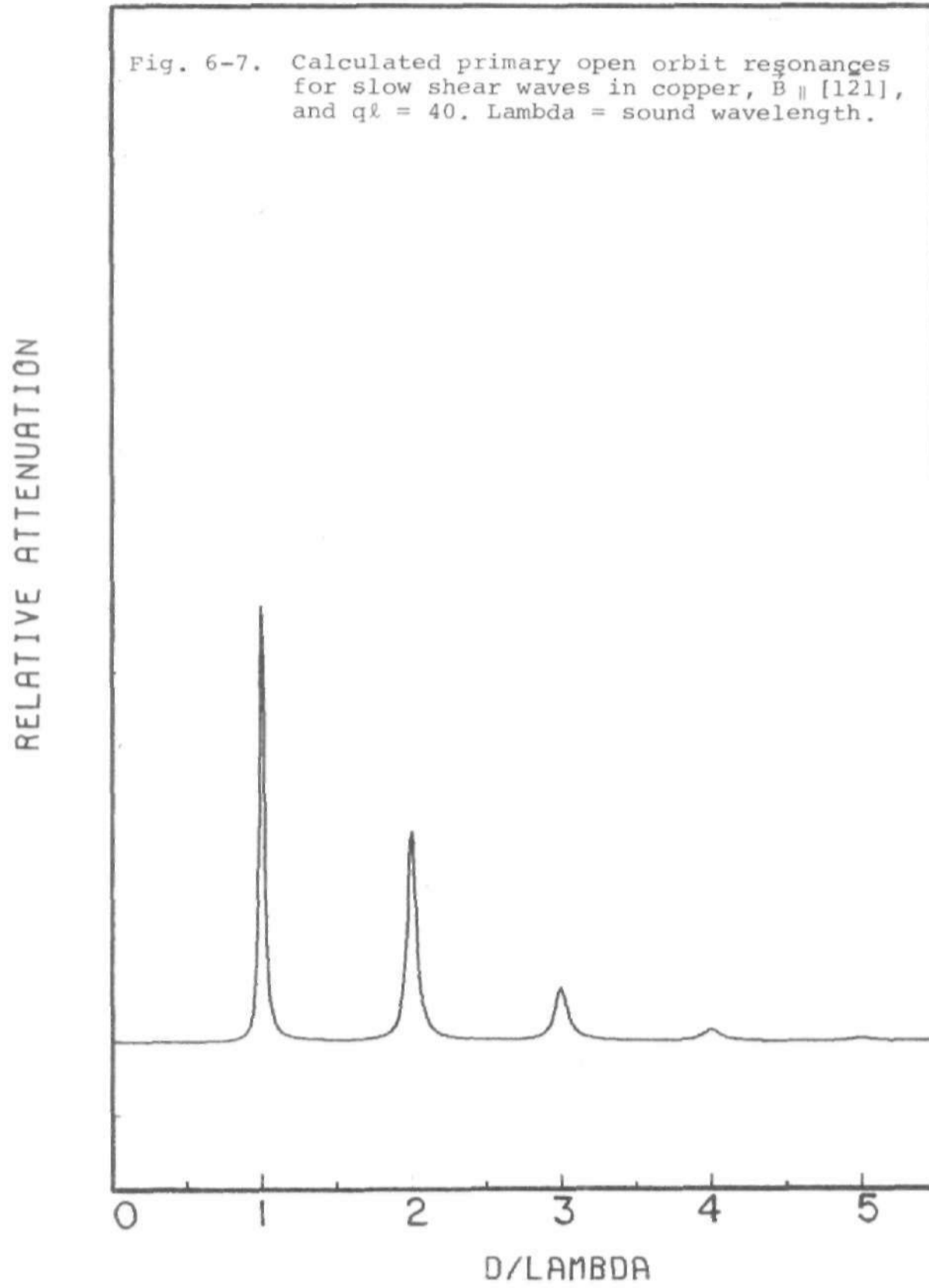


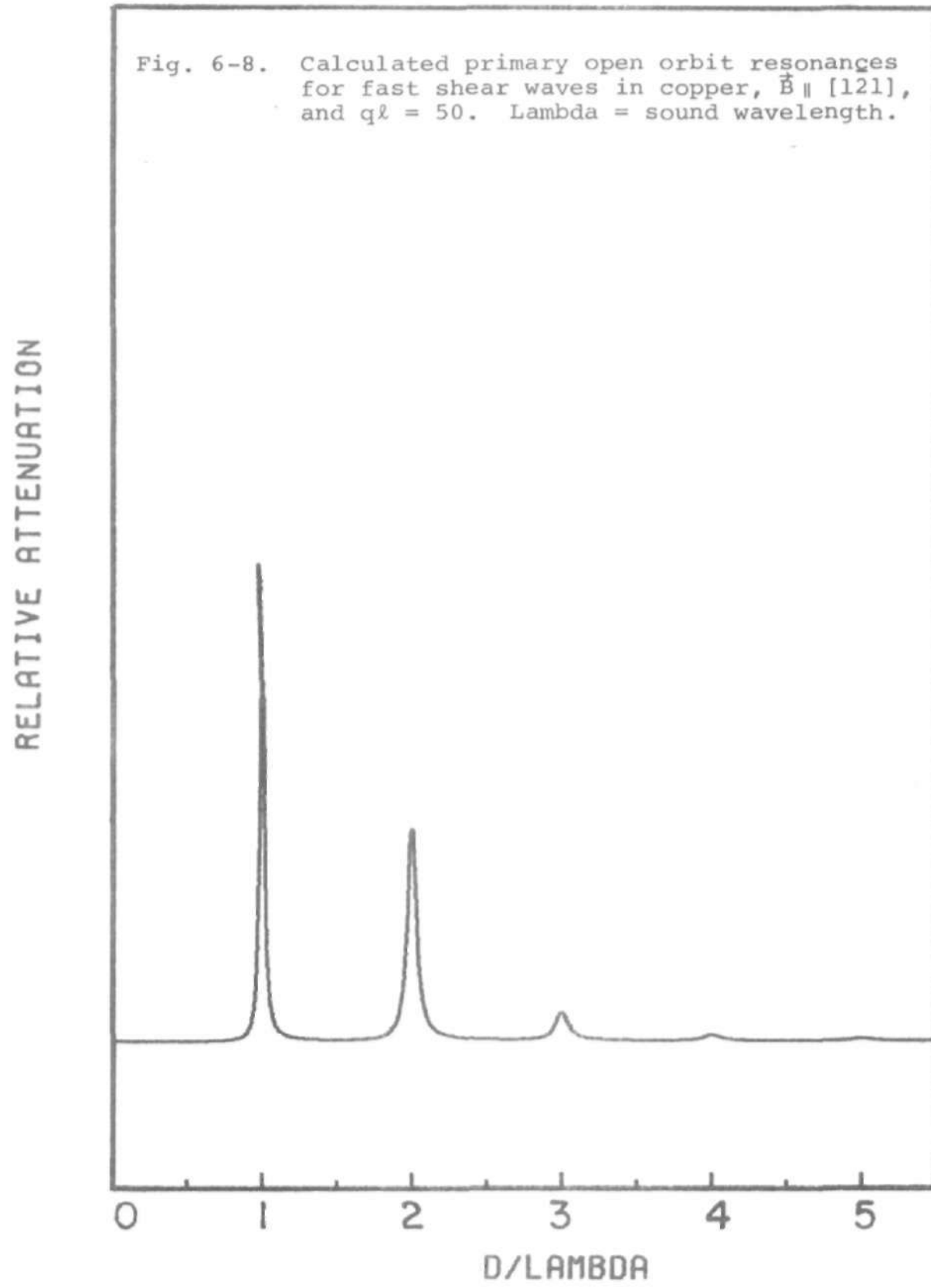
Fig. 6-6. Electron displacement on the secondary open orbit in gold.

whereas for $\vec{e}_{\parallel}[010]$, $(\vec{e}_{\perp}\vec{B})$, only the second harmonic is observed as shown in Fig. (5-10)

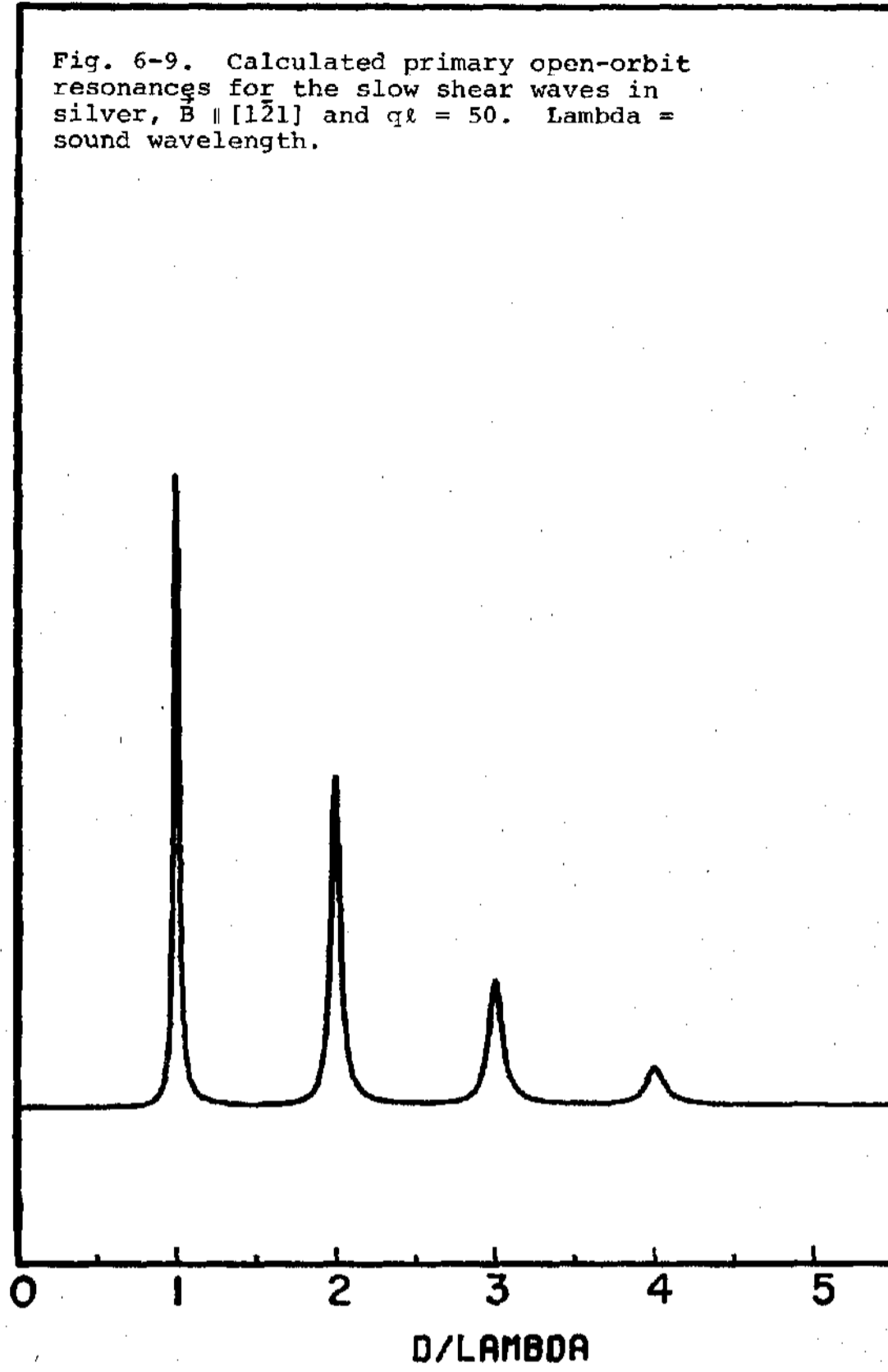
The relative heights of the resonances for each polarization direction observed in the experiments can be accounted for by calculating the attenuation in terms of the Fourier components of the effective force on the electrons and their velocities. In the calculations, the details of which are given in Chapter III, we have used the Fourier components of the electron velocities only, taking the effective force on the electrons to be simply proportional and parallel to the ion displacement. The results of the calculation for the primary open orbit are shown in Figs. (6-7)-(6-12), while Figs. (6-13)-(6-16) show the corresponding results of the calculation for the secondary open orbit. The results of the calculation are plotted in terms of the relative attenuation as a function of D/λ ($\sim 1/\lambda B$). In order to make an effective comparison, we have therefore replotted the experimental relative attenuation as a function of the reciprocal of the magnetic field \vec{B} . These graphs are shown in Figs. (6-17)-(6-25).

The experimental results can easily be explained by reference to the calculated results. For the primary open orbit, a series of resonance harmonics is obtained for both polarization directions, with subharmonics higher than the second one disappearing very rapidly (see Figs. (6-7)-(6-12)

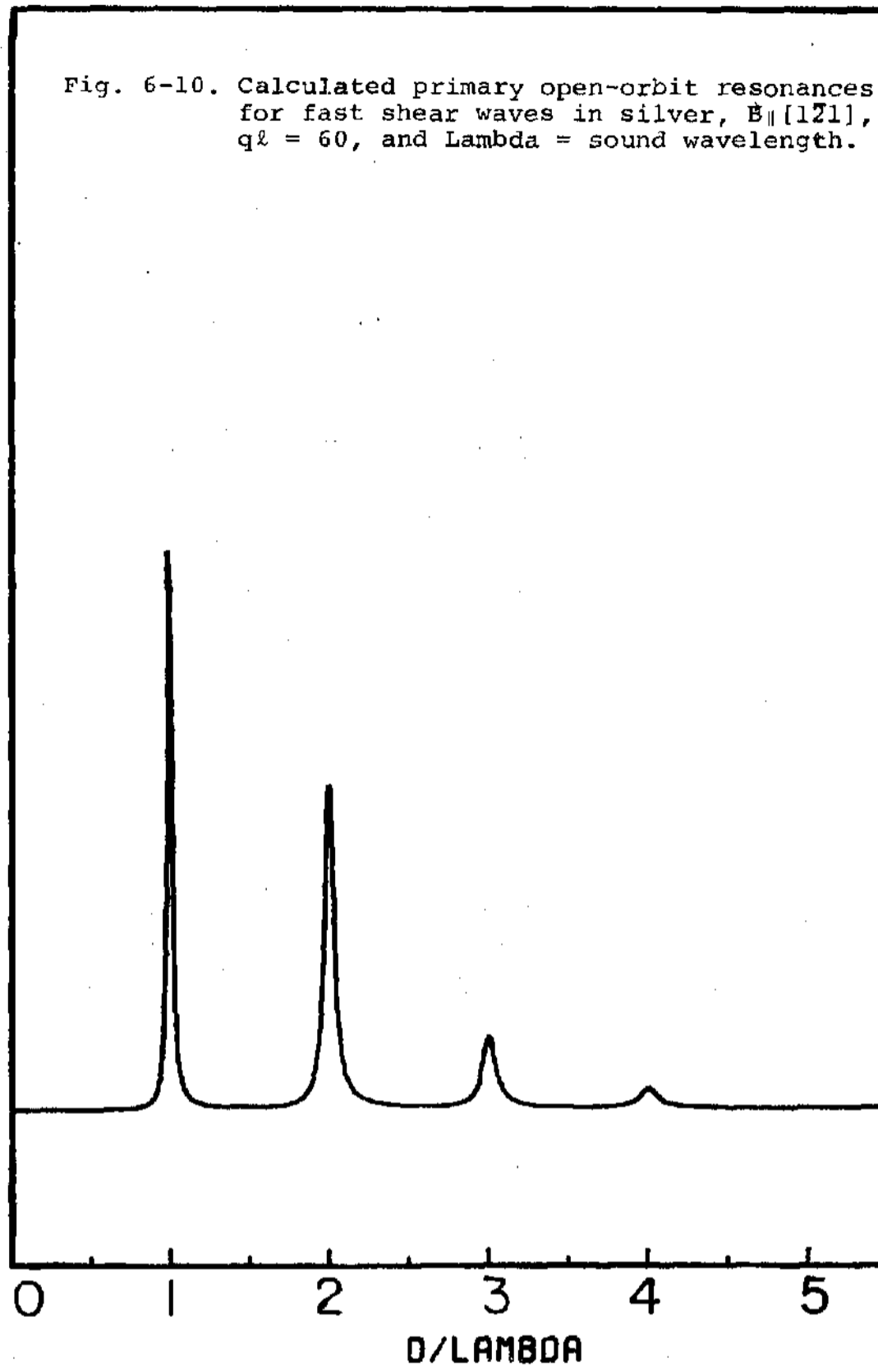




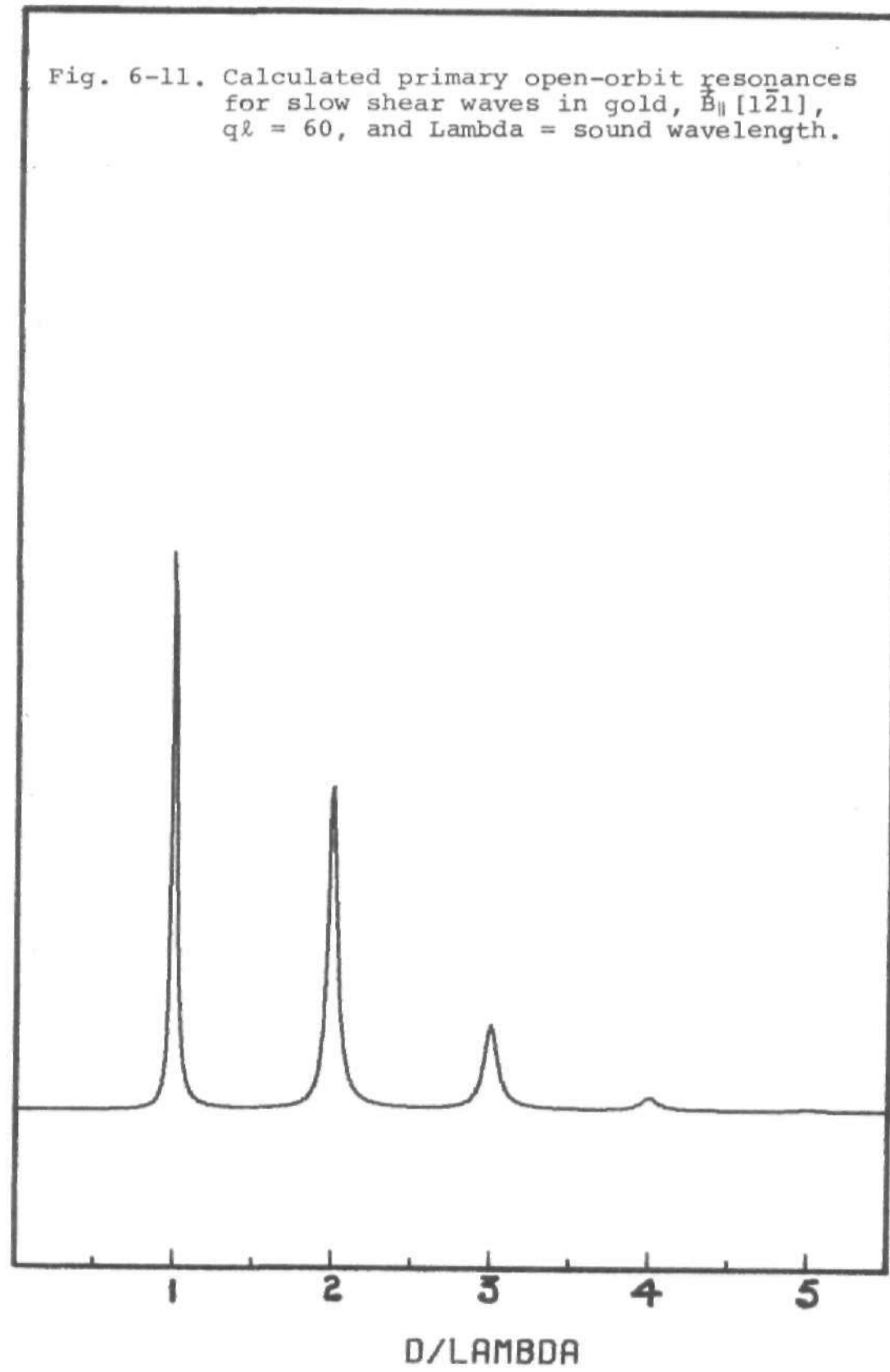
RELATIVE ATTENUATION



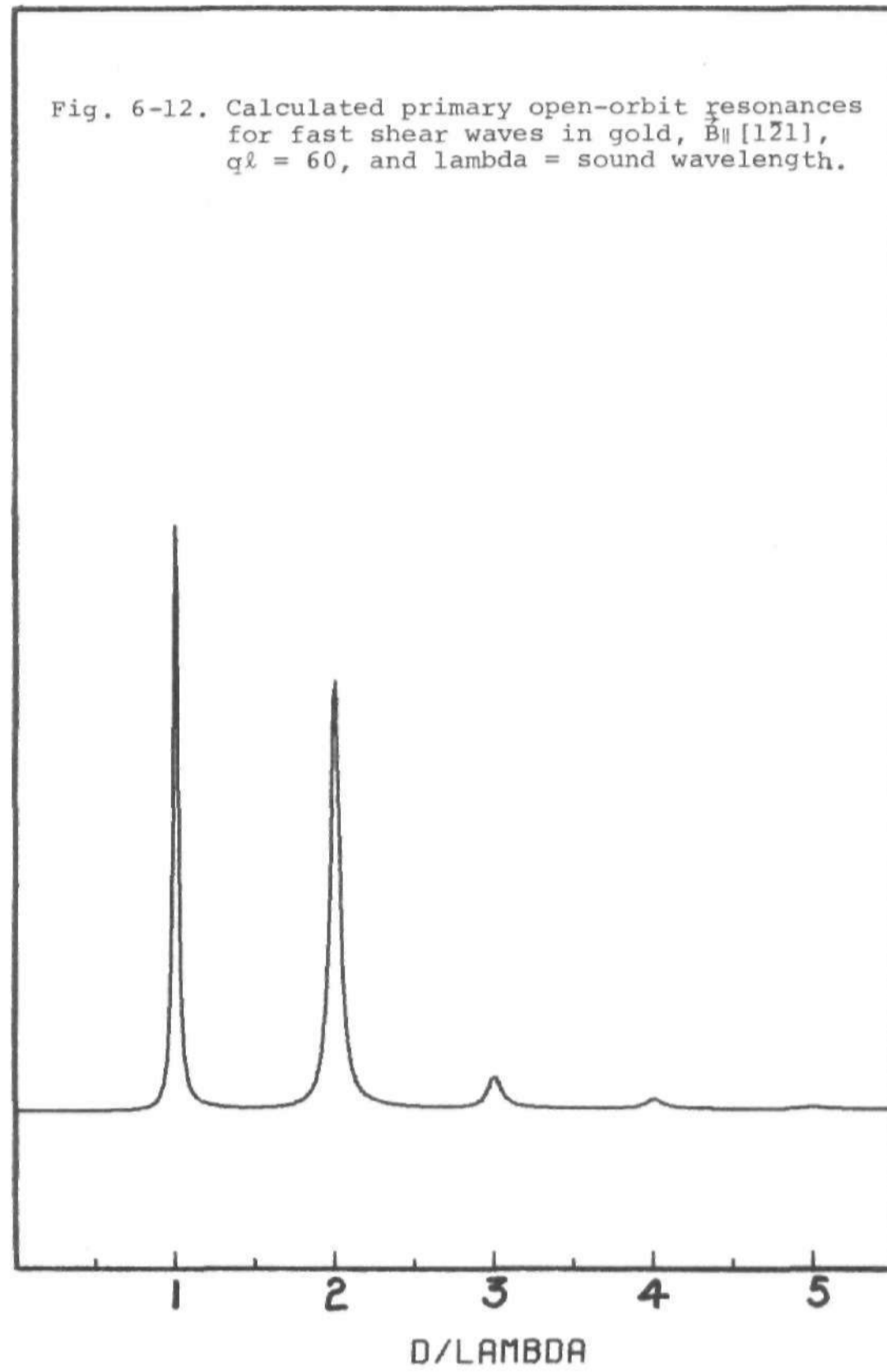
RELATIVE ATTENUATION



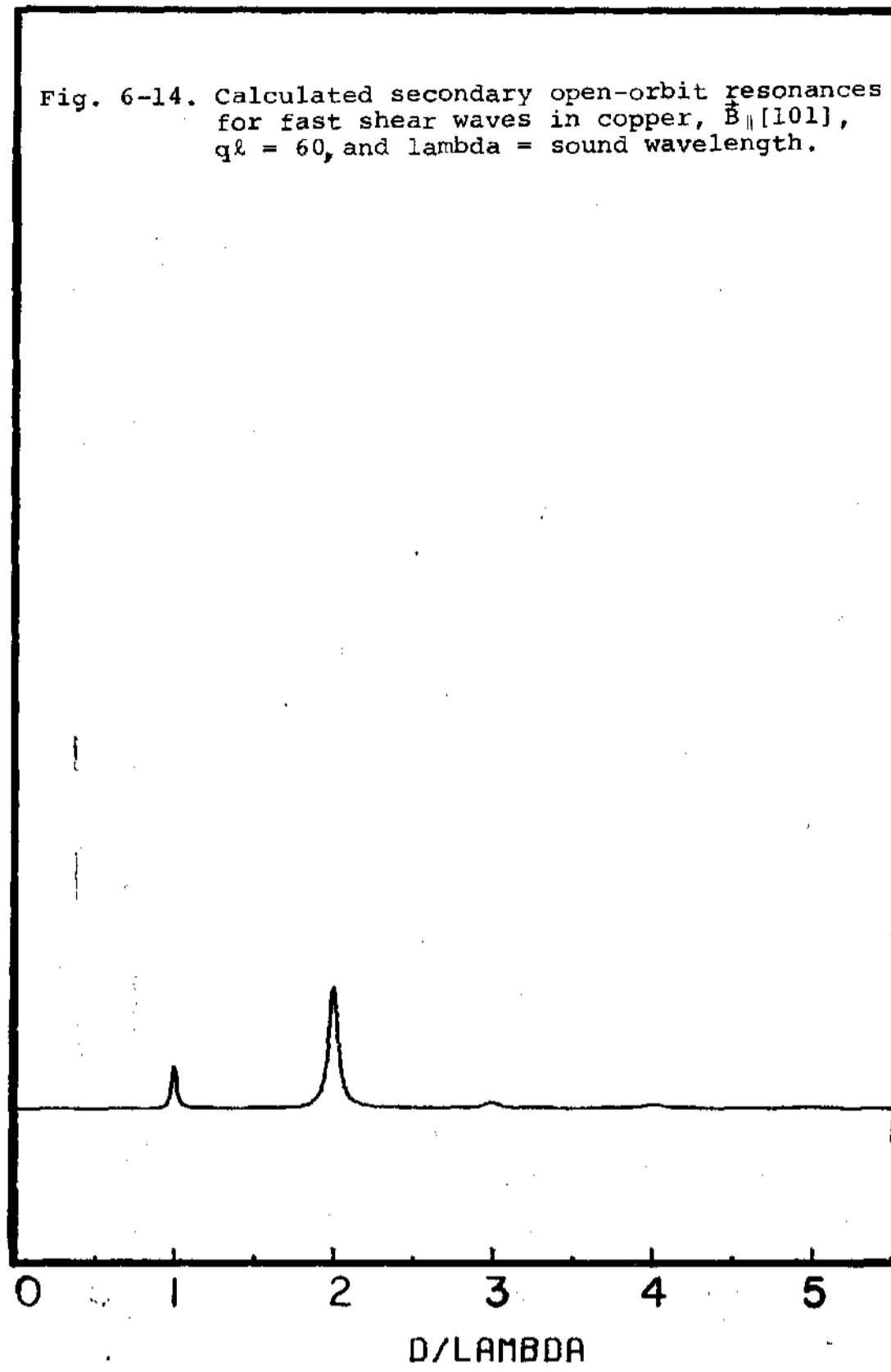
RELATIVE ATTENUATION



RELATIVE ATTENUATION



RELATIVE ATTENUATION



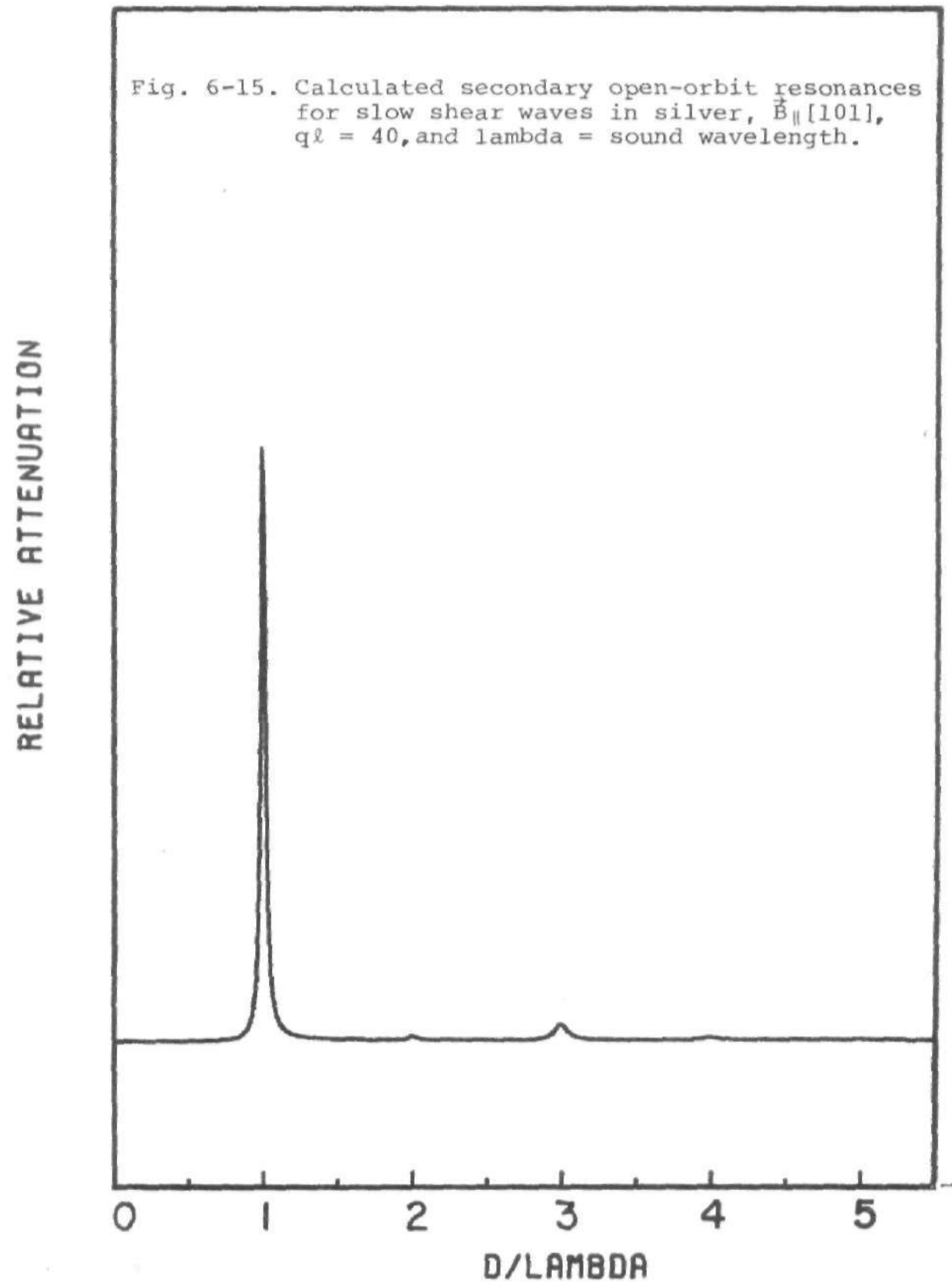
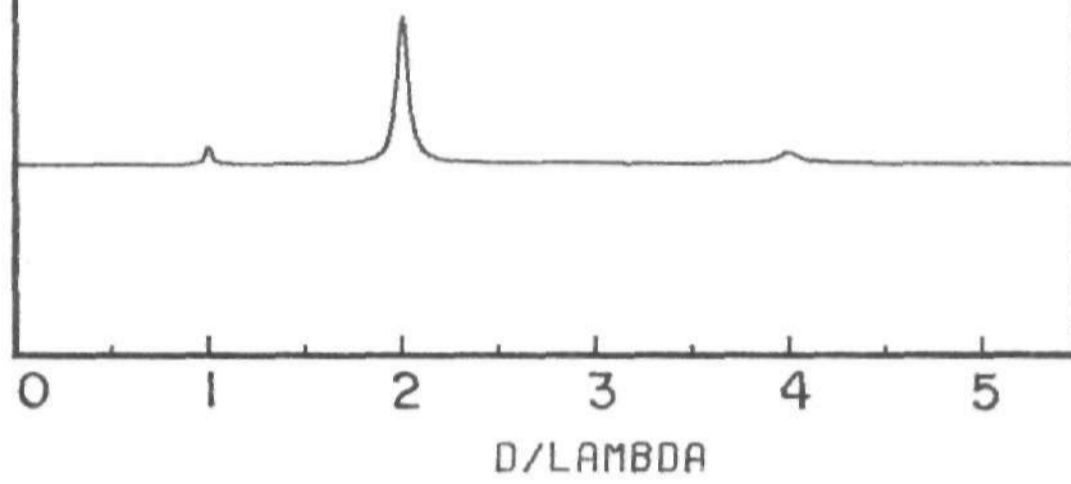
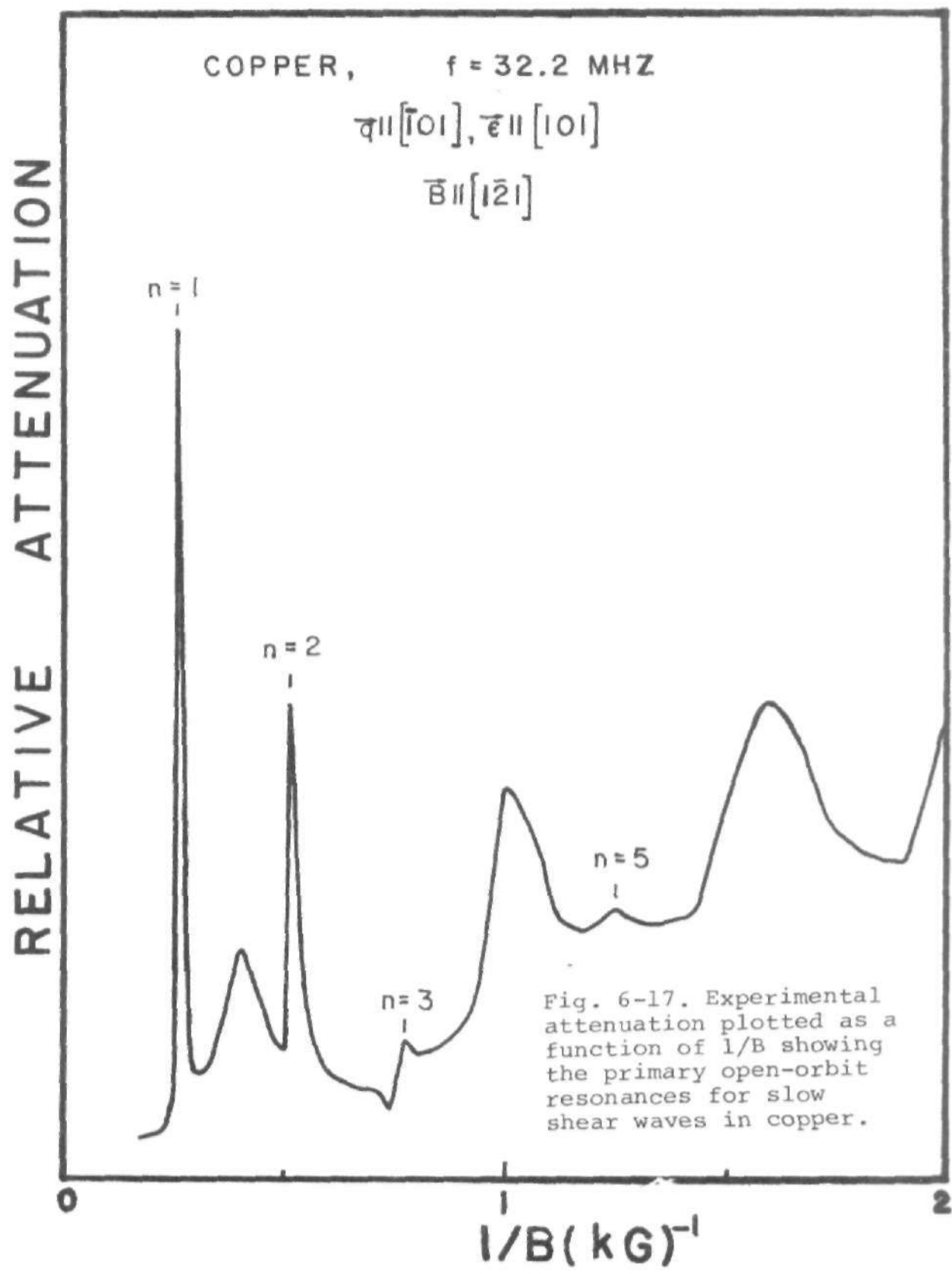


Fig. 6-16. Calculated secondary open-orbit resonances for fast shear waves in silver, $\vec{E} \parallel [101]$, $q\lambda = 40$ and $\lambda =$ sound wavelength.

RELATIVE ATTENUATION



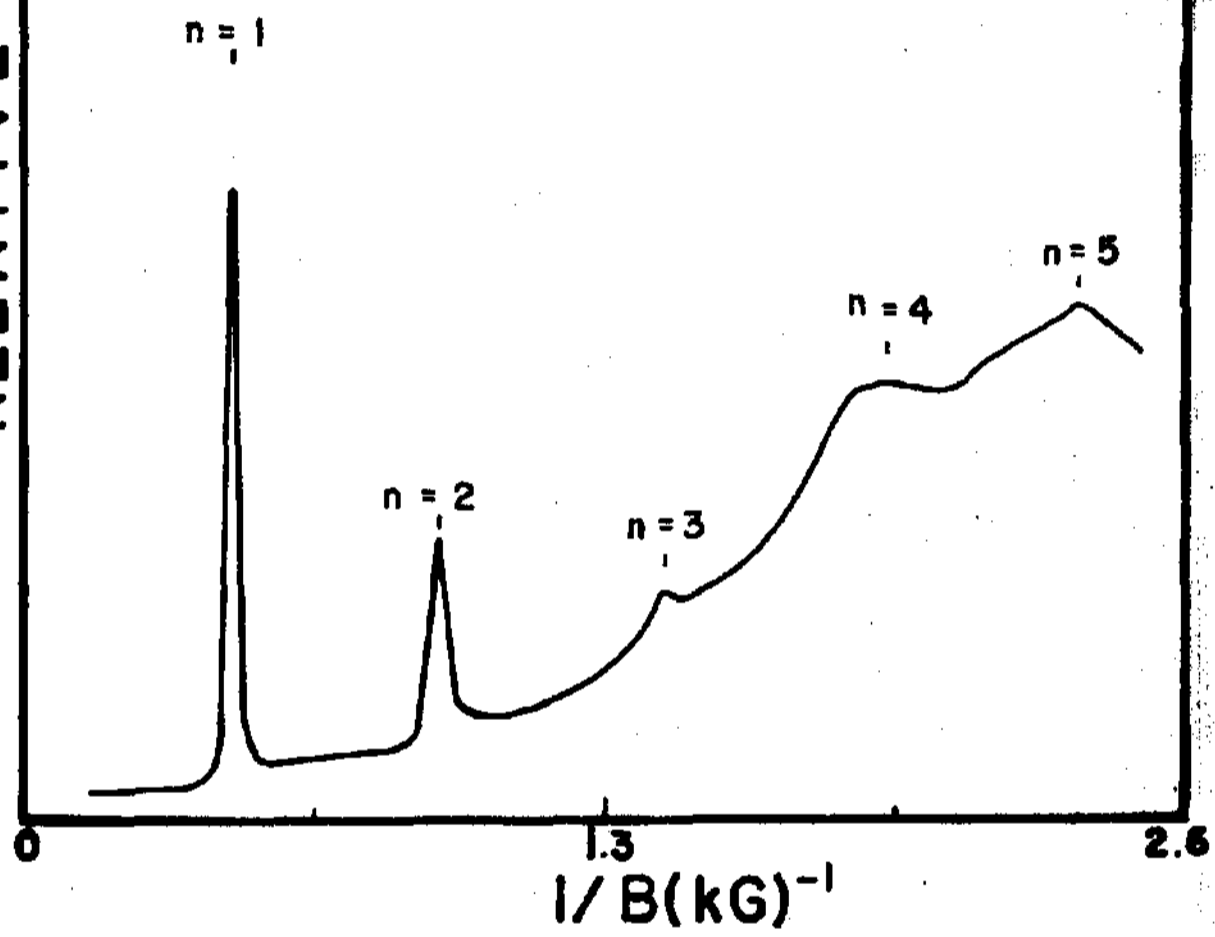


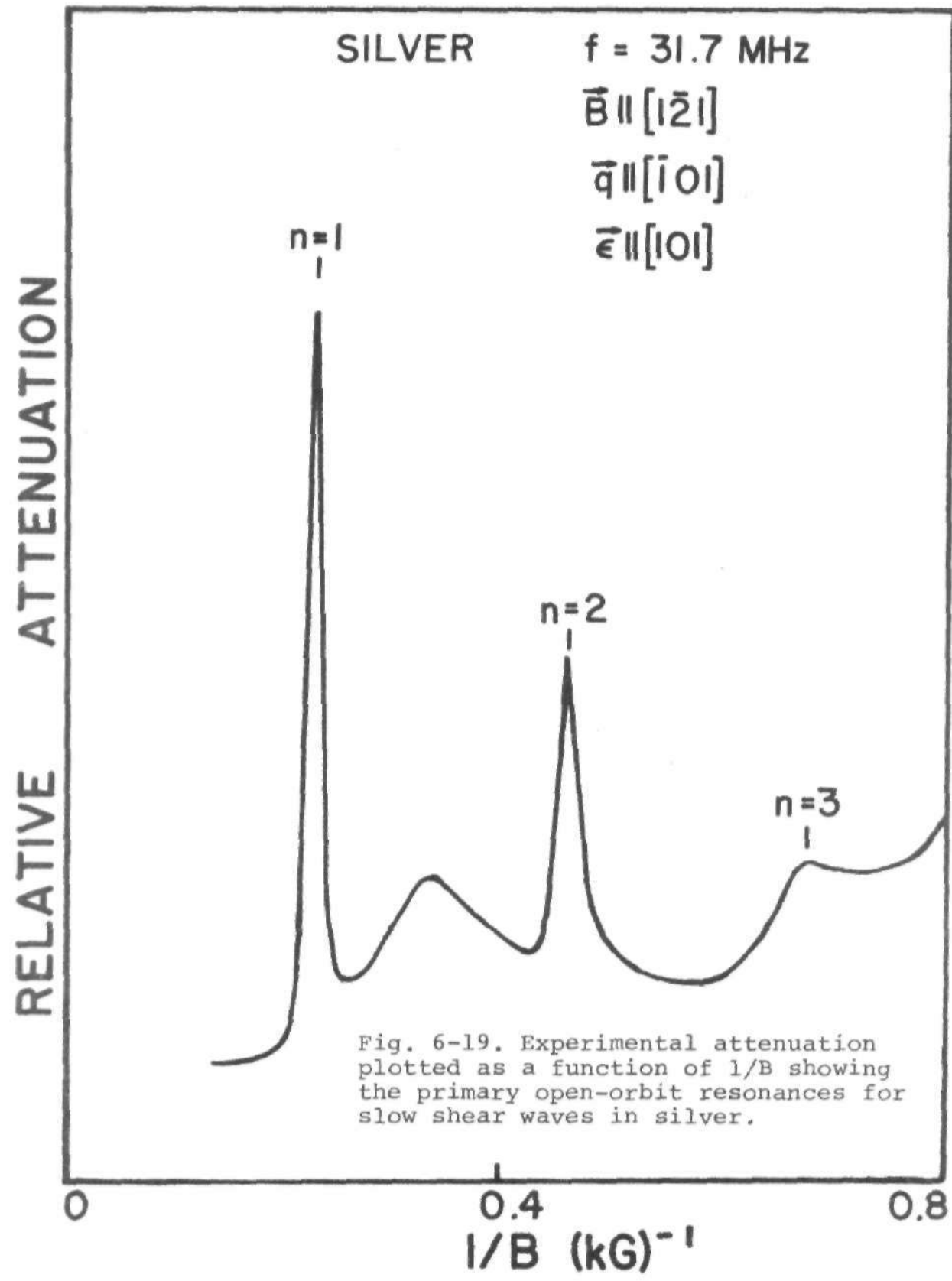
RELATIVE ATTENUATION

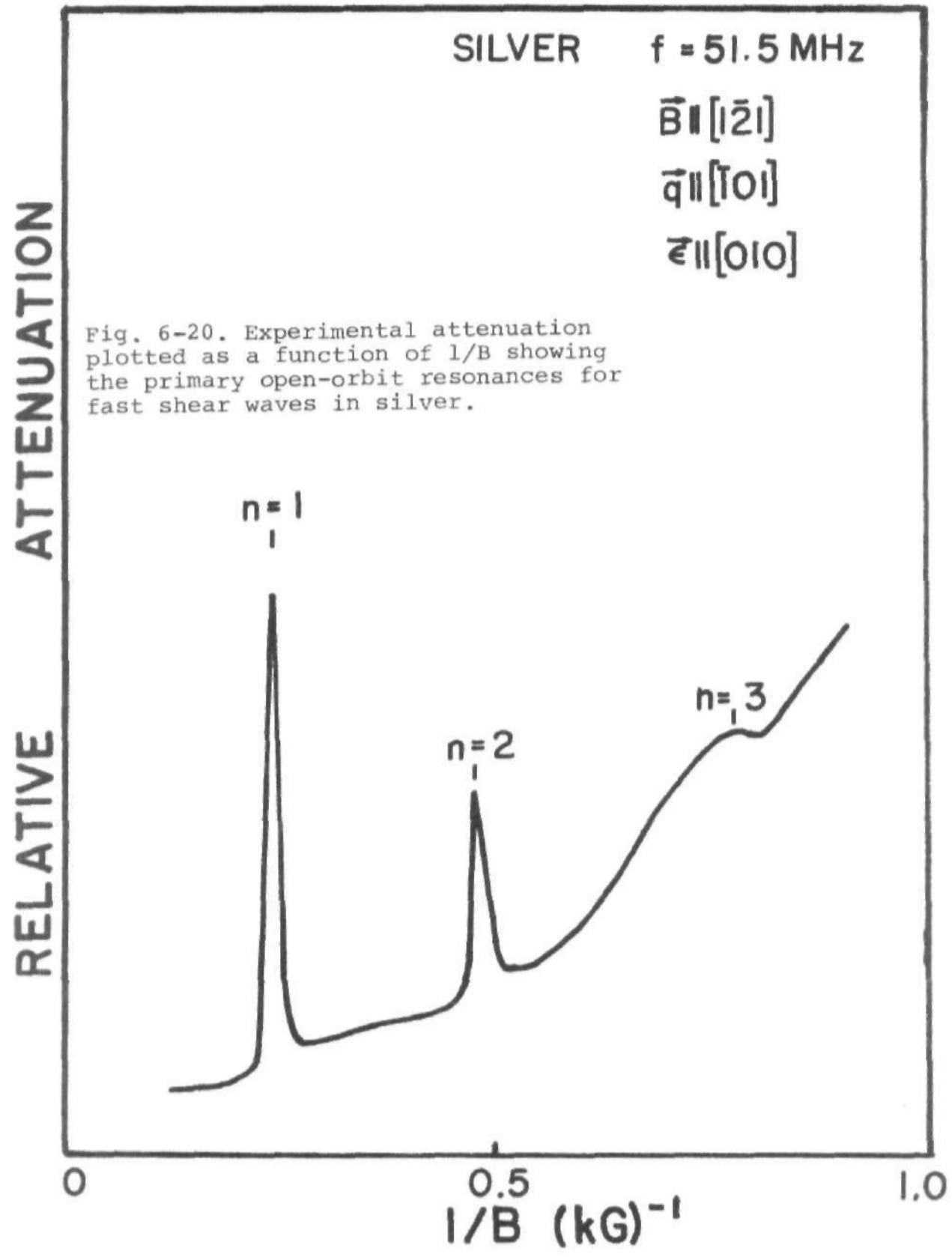
COPPER,

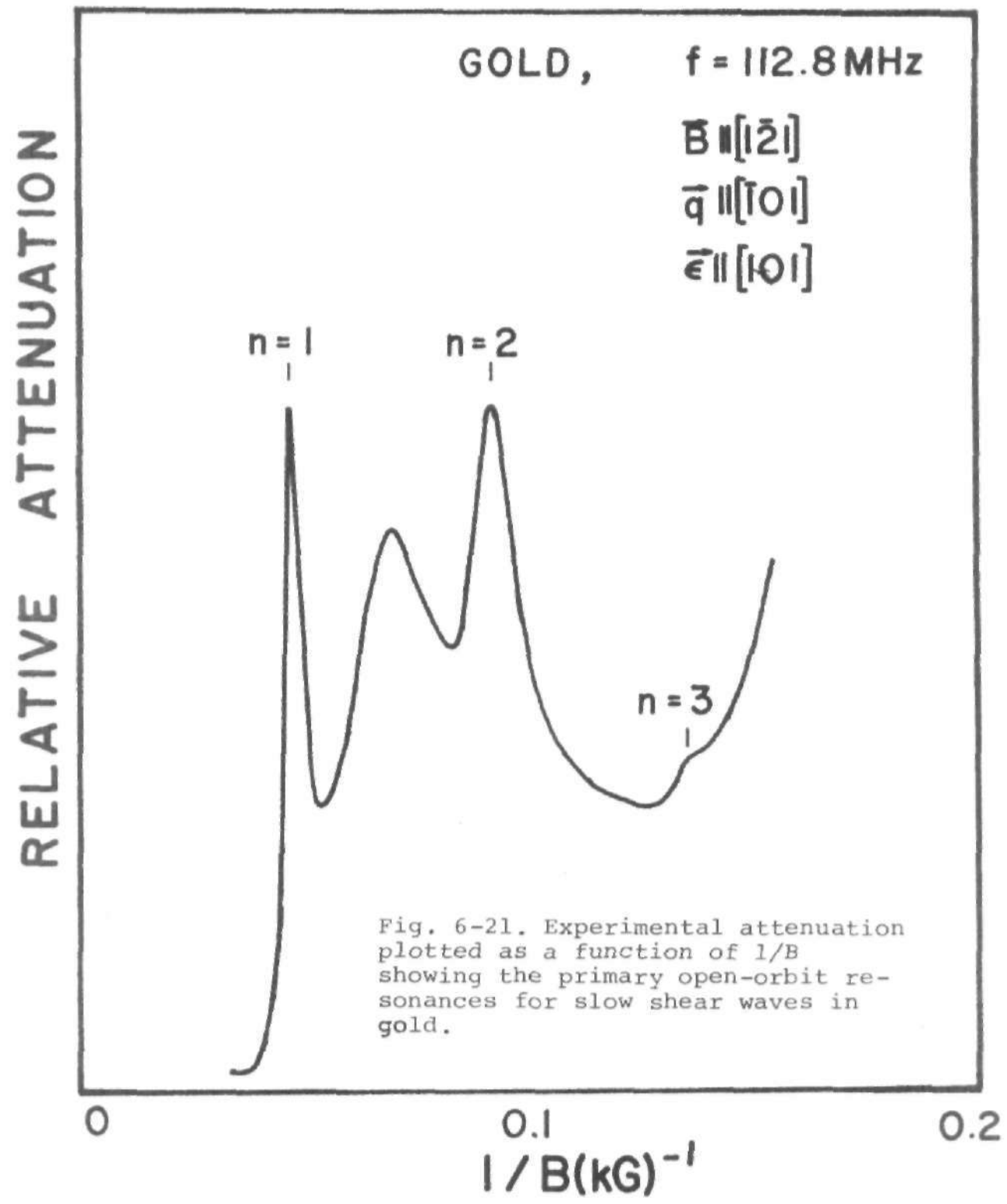
 $f = 32.2 \text{ MHz}$ $\vec{q} \parallel [101], \vec{E} \parallel [010], \vec{B} \parallel [1\bar{2}1]$

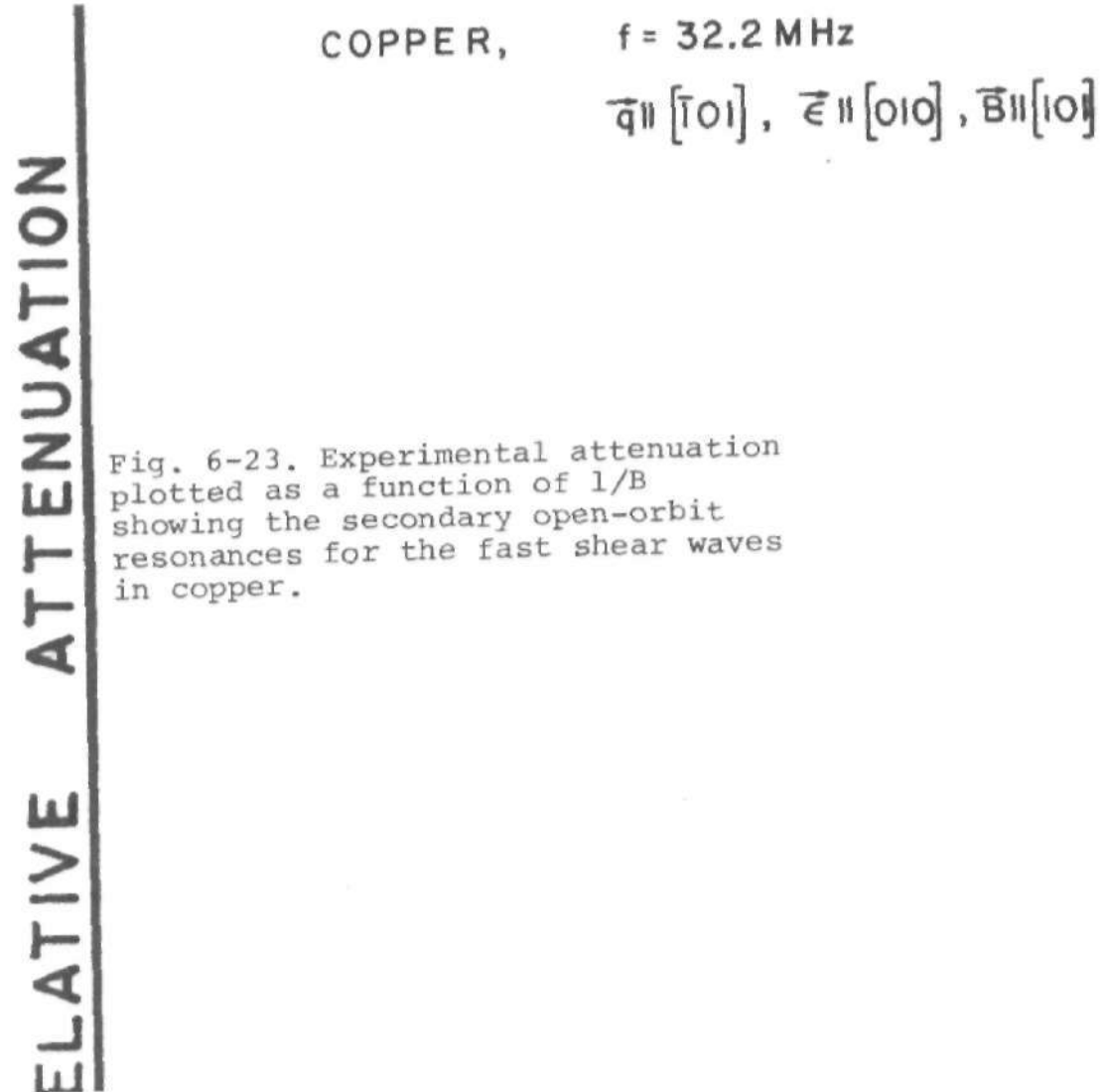
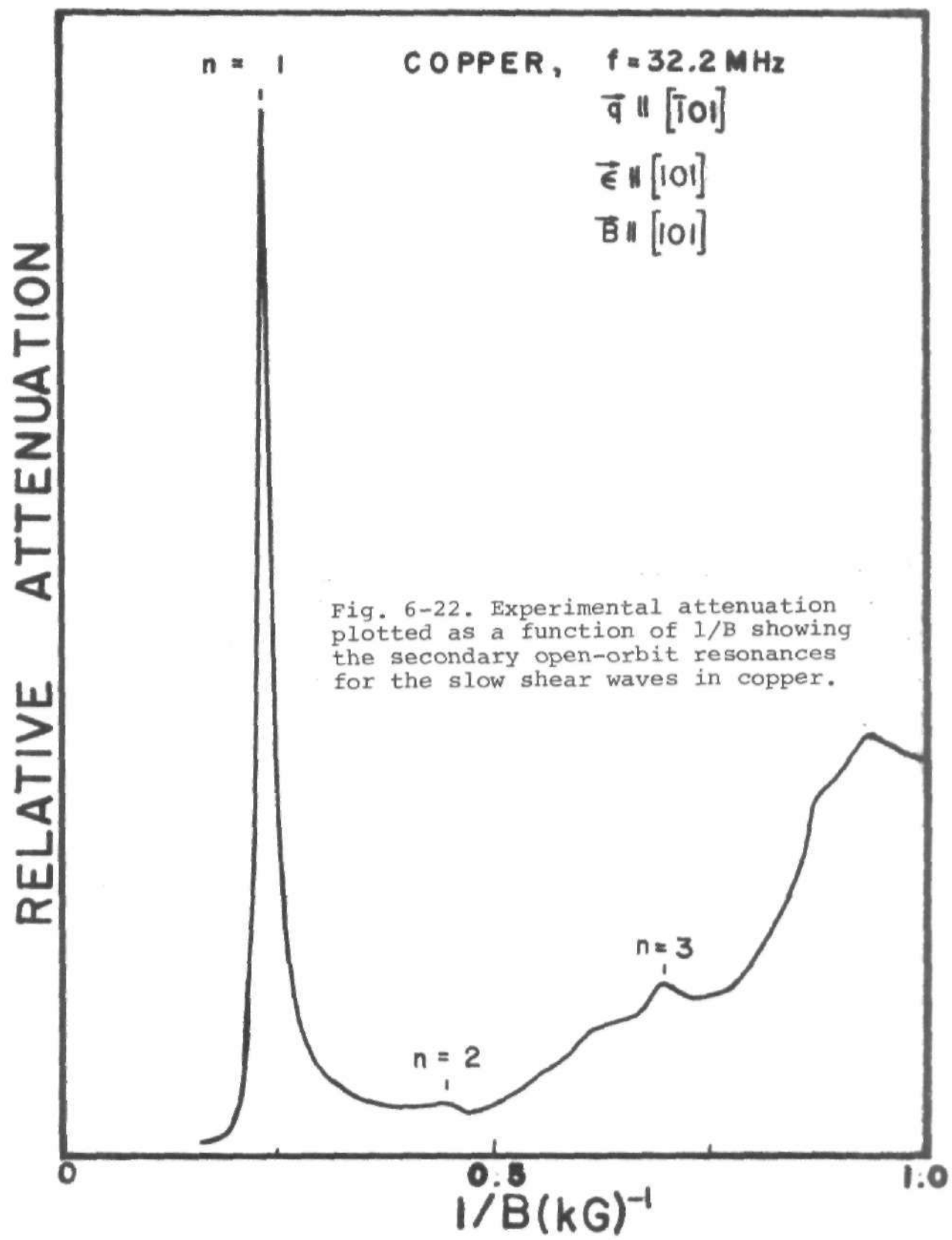
Fig. 6-18. Experimental attenuation plotted as a function of $1/B$ showing the primary open-orbit resonances for fast shear waves in copper.

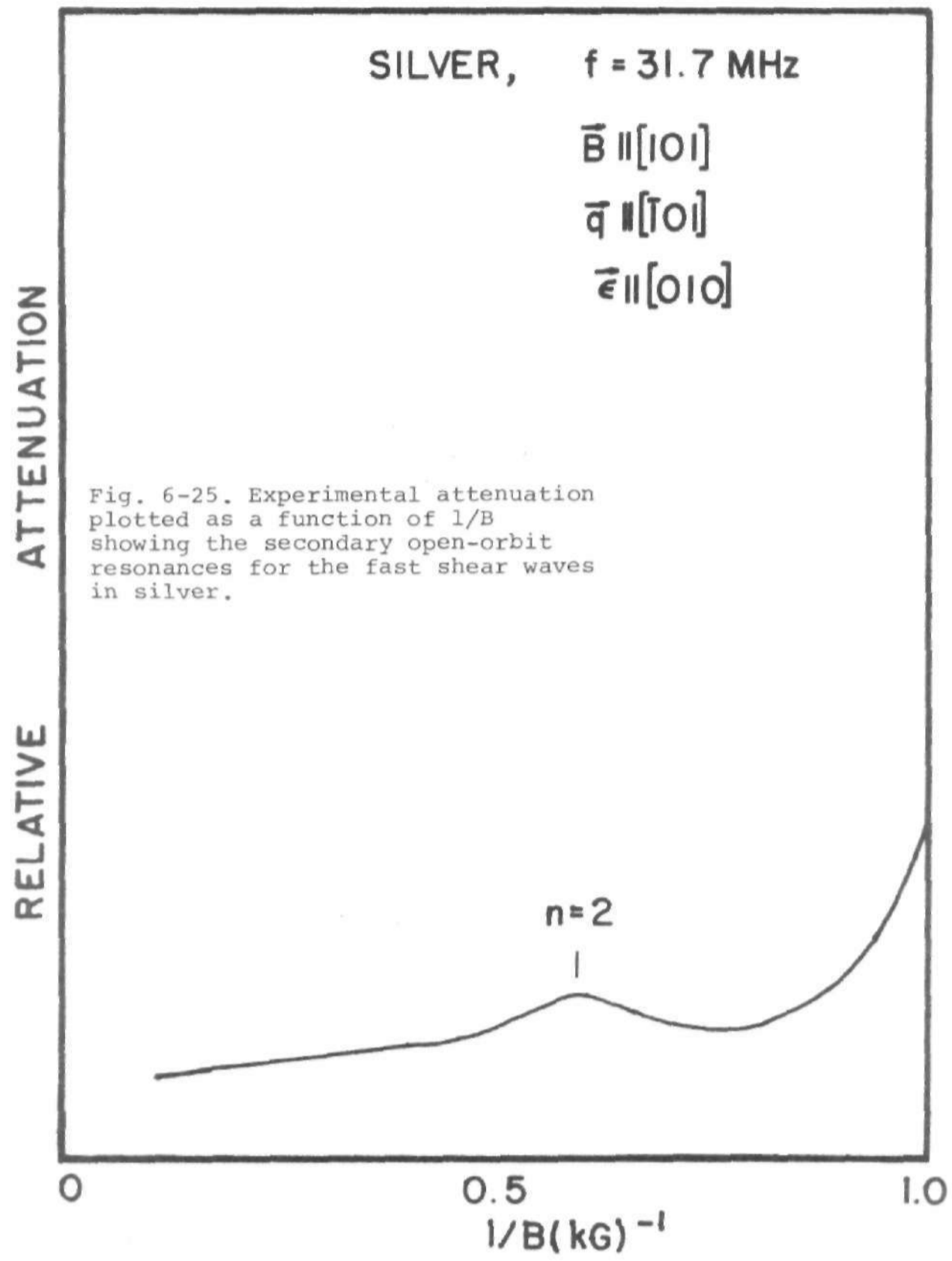












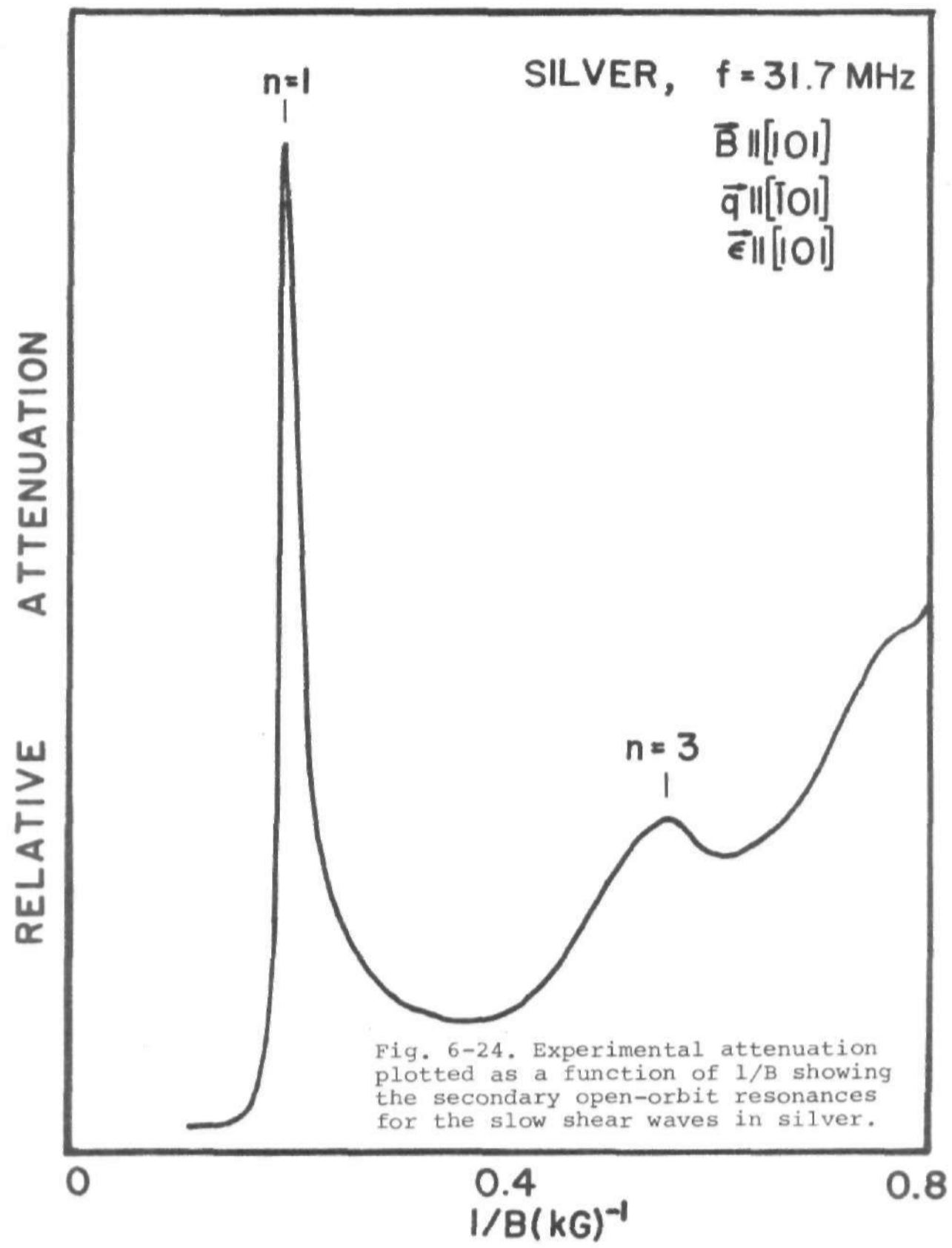


Table (6-1). Ratios of the heights of the fundamental (α_1) to those of the second harmonic (α_2) peaks from experimental and theoretical results.

Open Orbit	Experiment (α_1/α_2)		Theory (α_1/α_2)	
	Slow mode	Fast mode	Slow mode	Fast mode
<u>Copper</u>				
[111]	2.1±0.2	2.8± 0.4	2.1	2.5
[010]	117± 9	only second harmonic seen	116.0	first harmonic negligible
<u>Silver</u>				
[111]	2.1± 0.2	2.2± 0.5	2.0	1.8
[010]	second harmonic absent	only second harmonic seen	second harmonic negligible	first harmonic negligible
<u>Gold</u>				
[111]	1.8± 0.6	--	1.8	--

B. Compressional Wave Results

The relative heights of the open-orbit resonances obtained with compressional waves cannot be explained on the basis of the theory used to account for the shear wave results. This is because the assumptions about the effective force on the electrons are no longer valid. If we consider a compressional wave propagating along the x-axis, then the integral of Eq. (3.2) reduces to:

$$\begin{aligned}
 A_n &= \int_0^D \vec{F} \cdot \frac{d\vec{s}}{dx} e^{2\pi i n x/D} dx \\
 &= \int_0^D F_x \frac{dx}{dx} e^{2\pi i n x/D} dx \\
 &= \int_0^D F_x dx e^{2\pi i n x/D} \\
 &= 0, \text{ if } F_x \text{ is assumed constant. (D is} \\
 &\quad \text{the real space period of the open} \\
 &\quad \text{orbit.)}
 \end{aligned}$$

In order that this theory be applicable to the compressional wave, therefore, the detailed nature of the various components of the force (deformation potential, relative motion of the electrons on different parts of the Fermi surface, and electric field) must be taken into account.

... and $\lambda_{[111]} = (0.0026 \pm 0.0004)$ cm for gold. The fact that $\lambda_{[010]}$ is smaller than $\lambda_{[111]}$ by a factor of about 3 could be mainly a consequence of the smaller average velocity (by a factor of 2.8 for both copper and silver) of [010] open-orbit electrons.

Doppler-shifted open orbit resonances were observed with compressional waves in silver for $\vec{B} \parallel [101]$. These are associated with electrons traveling on a narrow band of open orbits running along the [010] direction. Similar Doppler-

shifted open-orbit resonances were observed in copper by Cox and Gavenda³⁹ and have been interpreted as being caused by the reduction of the electron velocity component along the propagation direction when the magnetic field is slightly rotated away from the [101] direction.

A theoretical calculation of the heights of the open-orbit resonances has been made for a simple phenomenological model using the Fourier components of the electron velocities and taking the force on the electrons to be proportional and parallel to the ion displacement. The calculations are based on the analytical expressions for the Fermi surfaces of the noble metals developed by Halse⁴¹. The results of the calculations are in good agreement with the experimental results. These results give useful information about the direction and characteristics of the effective force on the conduction electrons in the sound field. Since the attenuation is proportional to $\vec{F} \cdot \vec{v}$ integrated over a period of the open orbit, the fact that the principal features of the attenuation are determined by the component of \vec{v} along \vec{E} indicates that $F \parallel \vec{E}$.

The results of both calculations and experiments for the [010] open orbit in copper and silver reveal the importance of considering all the components of the motion of conduction electrons in magnetic transport phenomena, not just those perpendicular to \vec{B} . For this particular open

orbit, the resonant attenuation is much larger when \vec{e} and hence \vec{F} is parallel to \vec{B} than when \vec{F} is perpendicular to \vec{B} . The results demonstrate the inadequacy of the free electron theory in explaining magnetoacoustic effects, for the theory (CHH¹⁶) implies that oscillations in the attenuation should be larger for $\vec{e}_\perp \vec{B}$ than when $\vec{e}_\parallel \vec{B}$. Also, Sievert³⁷, using the free electron of CHH¹⁶ to calculate open orbit resonances for shear waves for cylindrical Fermi surfaces, obtained dips in the attenuation as a function of the magnetic field rather than peaks which are always seen in experiments. Finally, it is useful to note that experiments with shear waves provide more useful information than those with compressional waves because the open-orbit resonances in the attenuation are sharper and occur at field values where background attenuation is relatively small and constant.

standard functions whereupon (A-1) reduces to exactly the free electron equation of CHH¹⁶ (for $\lambda \rightarrow \infty$).

2. Case (j,k) - Shear wave in transverse field, $\vec{\epsilon} \parallel \vec{H}$.

$$\alpha_{jk} = \frac{e^2 H^2}{2\pi^2 \rho v_s \beta} \times \left\{ \frac{(I_{00} - I_{33})(I_{14} - P)^2 + 2I_{13}I_{34}(I_{14} - P) - I_{11}I_{34}^2}{I_{11}(I_{00} - I_{33}) + I_{13}^2} \right.$$

$$+ \frac{\beta^2}{2eH} \int dk_z \oint \lambda k_y^2 ds - I_{44}$$

$$+ \left[\frac{I_{15}(I_{10} - I_{33})(I_{15} + 2I_{14} - 2I_{35} - P)}{I_{11}(I_{00} - I_{33}) + I_{13}^2} \right. \quad (A-2)$$

$$\left. + I_{35} \frac{[I_{11}I_{35} - 2I_{13}I_{15} - 2(I_{00} - I_{33})(I_{14} - P)]}{I_{11}(I_{00} - I_{33}) + I_{13}^2} \right] \Bigg\}$$

where $P = \beta^2 V / (2\pi e H)$ and V is the volume enclosed by the Fermi surface.

It may be seen that in (A-2) all deformation effects are contained in the last term, since only η_5 and thus any I_{mn} with m and n equal to 5 contains the deformation parameter K . For the free electron model for a shear wave, $K=0$ so the last term in (A-2) vanishes. This term will also

vanish in a real metal with cubic symmetry when \vec{q} and \vec{e} are along cube axes, since reflection symmetry causes the two conjugate orbits to make contributions to I_{mn} which just cancel each other.

3. Case ($\underline{k}, \underline{k}$) - Shear wave in transverse field, $\vec{e} \parallel \vec{H}$.

$$\alpha_{kk} = \frac{e^2 H^2}{2\pi^2 \rho v_s \beta^2} \left\{ I_{0'0'} - I_{66} + \frac{(I_{26} + P)^2}{I_{22}} + (I_{55} - \frac{I_{25}^2}{I_{22}}) \right\}, \quad (A-3)$$

where $I_{0'} = \beta k_z I_0$.

When the mean free path of the electrons is comparable to the sound wavelength (or $q\ell \approx 1$), the integrals I_{mn} show oscillatory behavior. The various I_n (except I_0) can be expressed in terms of Bessel functions which leads to oscillatory dependence of the attenuation on the magnetic field.

APPENDIX B

Mertching's Results for the Attenuation Coefficient

Mertching's results for the attenuation coefficient in general can be expressed as

$$\alpha = \frac{1}{\rho v_s} \operatorname{Re}(K_{ss}),$$

where $s=1,2,3$ specifies the direction of polarization of the sound wave, ρ is the density of the metal, and K_{ss} is the diagonal element of the effective force tensor \underline{K} . The expression for \underline{K} is very complicated, but its main features can be seen by considering the form of α for compressional waves propagating along an axis of high symmetry:

$$\alpha_L = \frac{\omega}{2\pi^2 \hbar^2 v_L^3 \rho_0} \operatorname{Re} \int m_c Q \sum_{n=-\infty}^{\infty} \frac{|\Lambda_n|^2 dk_z}{\tau^{-1} + i(\vec{q} \cdot \vec{v} - \omega - n\omega_c)},$$

$$\text{where } \Lambda_n = \frac{1}{2\pi} \int_0^{2\pi} \Lambda_L(\theta) e^{-i/\omega_c} \int_0^\theta \vec{q} \cdot [\vec{v} - \langle \vec{v} \rangle] d\theta' - i n \theta \quad (\text{B-1})$$

v_L = longitudinal sound velocity,

k_z = component of electron wave vector along the field \vec{B} ,

Q = a quantum factor which reduces to 1 in the quasiclassical magnetic-field range, $\hbar\omega_c \ll kT$.

$\langle \vec{v} \rangle$ = average velocity of an electron over a cyclotron orbit,

θ = angle coordinate for electron cyclotron orbits on the Fermi surface,

$\overline{\tau^{-1}}$ = reciprocal of electron relaxation time averaged over a cyclotron orbit,

$\Lambda_L(\theta)$ = longitudinal component of the deformation force.

All the resonance and oscillation phenomena discussed in Chapter II are contained in this expression (B-1).

APPENDIX C

Further Details of the Program Orbit

We consider here the details of the calculation of the gradients of Halse's function for the noble metals represented in Eq. (3-22). We first find a point on the surface and step around an orbit in equal time intervals, making sure that the orbit remains in a plane perpendicular to \vec{B}_0 . The number of steps to get around an orbit is proportional to the cyclotron period T_c , and hence to the cyclotron mass m_c .

In order to find the starting point on the surface, we locate two points lying in the plane $k_z = \text{constant}$ (the magnetic field is taken in the z-direction for convenience). One of these points is on the k_z axis and the other is on the zone boundary or at some other point known to be just outside the Fermi surface. These points are so chosen so that the line joining them intersects the surface defined by $W(\vec{k}) = W_f(\vec{k} = k_x \underline{i} + k_y \underline{j} + k_z \underline{k})$. We may therefore find the root of the equation by iterating back and forth along the starting line using the method of False Position⁴⁷. We continue the iteration until $|W(\vec{k}) - W_f| \leq 10^{-8}$ or until 100 iterations have been made. This gives the components of the electron wave-vector \vec{k}_f .

An electron with momentum $\hbar\vec{k}$ and velocity \vec{v} will move in a magnetic field \vec{B}_0 in such a way that $\hbar\dot{\vec{k}} = e(\vec{v} \times \vec{B}_0)/c$; consequently successive values of \vec{k} are given by integrating $(\vec{v} \times \vec{B}_0)$ with respect to time, i.e.,

$$\vec{k}_{n+1} = \vec{k}_n + \int_t^{t+\Delta t} \frac{e}{\hbar c} (\vec{v} \times \vec{B}_0) dt. \quad (C-1)$$

This equation may be written in dimensionless form as

$$\vec{R}_{n+1} = \vec{R}_n + \left(\frac{\partial W}{\partial \vec{R}} \times \vec{B}_0 \right) \Delta t', \quad (C-2)$$

where $\Delta t' = (Kea^2/ch^2)\Delta t$. K is a parameter relating E_f to W_f .

To check that a point \vec{R}_n ($n=1,2,3,\dots$) is on the surface, it is only necessary to compute $E(\vec{R}_n)$ and confirm that it is, within a specified small tolerance, equal to E_f . If it is not, replacement of \vec{R}_n by

$$\vec{R}'_n = \vec{R}_n - \frac{\Delta W \left[\frac{\partial W}{\partial \vec{R}} - \left(\frac{\partial W}{\partial \vec{R}} \cdot \hat{B}_0 \right) \hat{B}_0 \right]}{\left[\left| \frac{\partial W}{\partial \vec{R}} \right|^2 - \left(\frac{\partial W}{\partial \vec{R}} \cdot \hat{B}_0 \right)^2 \right]} \quad (C-3)$$

gives, by Newton's method, a point with the same value of R_B (component of \vec{R} parallel to the field) which should be a better approximation. We iterate using Eq. (A-6) until

$|W_{\vec{f}} - W(\vec{R})| \leq 10^{-8}$ and continue to step around the orbit computing \vec{R}_n and the corresponding gradients at the surface.

We need to recognize the starting point so that we can stop the scan. If $|\vec{R}_n - \vec{R}_1| < |\vec{R}_2 - \vec{R}_1|$, then the orbit is complete. If not, we must check for an open orbit. We assume that if the orbit has not closed after traveling 50 reciprocal lattice vectors, it is an open orbit.

Having completed the orbit, we then determine how many steps N it took to get around it. We know that $m_c \propto N$. In the case of an open orbit, we define N to be the number of steps it takes to travel over one period of the orbit.

BIBLIOGRAPHY

1. H. E. Bömmel and J. L. Olsen, Phys. Rev. 91, 1017 (1953).
2. H. E. Bömmel, Phys. Rev. 96, 220 (1954).
3. L. Mackinnon, Phys. Rev. 100, 655 (1955).
4. W. P. Mason, Phys. Rev. 97, 557 (1955).
5. R. W. Morse, Phys. Rev. 97, 1716 (1955).
6. A. B. Pippard, Phil. Mag. 46, 1104 (1955).
7. H. E. Bömmel, Phys. Rev. 100, 758 (1955).
8. R. W. Morse, Bull. Am. Phys. Soc. Ser. II, 1, 300 (1956).
9. A. B. Pippard, Phil. Mag. 2, 1147 (1957).
10. T. Holstein, Westinghouse Research Memo 60-94698-3 M17 (1956).
11. R. W. Morse, H. V. Bohm, and J. D. Gavenda, Phys. Rev. 109, 1394 (1958).
12. R. W. Morse and J. D. Gavenda, Phys. Rev. Lett. 2, 250 (1959).
13. S. Rodriguez, Phys. Rev. 112, 80 (1958).
14. T. Kjeldaas and T. Holstein, Phys. Rev. Lett. 2, 340 (1959).
15. T. Kjeldaas, Phys. Rev. 113, 1473 (1959).
16. M. Cohen, M. J. Harrison, and W. A. Harrison, Phys. Rev. 117, 937 (1960).
17. A. B. Pippard, Proc. Roy. Soc. 257, 165 (1960).
18. V. L. Gurevich, Zh. Eksperim. i Teor. Fiz. 37, 71 (1959);

- 37, 1680 (1959) [English translation: Soviet Phys.-JETP 10, 1190 (1960); 10, 1190 (1960)].
19. A. I. Akhiezer, M. I. Kaganov, and G. I. Lyubarskii, Zh. Eksperim. i Teor. Fiz. 32, 837 (1957) [English transl.: Soviet Phys. JETP 5, 685 (1957)].
 20. E. A. Kaner, Zh. Eksperim. i Teor. Fiz. 39, 1071 (1960) [English transl.: Soviet Phys.-JETP 12, 747 (1961)].
 21. A. A. Galkin, E. A. Kaner, and A. P. Korolyuk, Zh. Eksperim. i Teor. Fiz. 39, 1517 (1960): Doklady Akademii Nauk SSSR 134, 74 (1960) [English transl.: Soviet Phys.-JETP 12, 1055 (1962); Soviet Phys.-Dokl. 5, 1002 (1961)].
 22. E. A. Kaner, V. G. Peschanskii, and I. A. Privorotskii, Zh. Eksperim. i Teor. Fiz. 40, 214 (1961) [English transl.: Soviet Phys.-JETP 13, 147 (1961)].
 23. H. Stolz, phys. stat. sol. 3, 1153 (1963); 3, 1493 (1963), 3, 1957 (1963), 9, 3 (1965).
 24. J. Mertsching, phys. stat. sol. 14, 3 (1966).
 25. J. Mertsching, phys. stat. sol. 16, 267 (1966).
 26. J. Mertsching, phys. stat. sol. 37, 465 (1970).
 27. L. Kleinman, Phys. Rev. 182, 686 (1969).
 28. C. R. Oré-Oré and L. Kleinman, Phys. Rev. 4, 4372 (1971).
 29. L. Onsager, Phil. Mag. 43, 1006 (1952).
 30. A. B. Pippard, The Dynamics of Conduction Electrons. Gordon and Breach, New York (1965).
 31. B. W. Roberts, Phys. Rev. 119, 1889 (1960).

32. C. W. Burmeister, D. B. Doan, and J. D. Gavenda, Phys. Rev. Letters 7, 112 (1963).
33. G. N. Kamm and H. V. Bohm, Phys. Rev. 131, 111 (1963).
34. B. C. Deaton and J. D. Gavenda, Phys. Rev. 136, A 1096 (1964).
35. P. R. Sievert, Phys. Rev. 161, 637 (1967).
36. Y. Eckstein, J. B. Ketterson, and M. G. Priestly, Phys. Rev. 148, 586 (1966).
37. L. R. Testardi and R. R. Soden, Phys. Rev. 158, 581 (1967).
38. J. A. Munarin, Phys. Rev. 172, 737 (1968).
39. W. R. Cox and J. D. Gavenda, Phys. Rev. B 3, 231 (1971).
40. J. D. Gavenda and W. R. Cox, Phys. Rev. B (To be published).
41. M. R. Halse, Phil. Trans. Roy. Soc. (London) A265, 507 (1969).
42. D. J. Roaf, Phil. Trans. Roy. Soc. A255, 135 (1962).
43. L. T. Wood, Ph. D. Thesis, University of Texas, 1968, (Unpublished).
44. W. R. Cox, Ph. D. Thesis, University of Texas, 1970, (Unpublished).
45. D. Shoenberg, Phil. Trans. Roy. Soc. (London) A255, 85 (1962).
46. J. J. Gniewek and A. F. Clark, J. Appl. Phys. 36, 3358 (1965).
47. K. S. Kunz, Numerical Analysis. McGraw-Hill Book Co., New York (1957).



VITA

Moses Egene Adah, son of Okeme and Ajimi Abutu, was born in Ogodu, Nigeria, on August 23, 1939. After completing his secondary school education at Okene Provincial Secondary School in 1960, he entered Keffi Government College in 1961 and then proceeded to Ahmadu Bello University, Zaria, Nigeria, in September, 1963. He was awarded the degree of Bachelor of Science (Combine Hons.) in Mathematics and Physics in June, 1966. He entered the Graduate School of the University in October, 1966, and was awarded the degree of Master of Science in January, 1968. He was appointed Assistant Lecturer in Physics at Ahmadu Bello University, Zaria, Nigeria, in October, 1967. In September, 1969, he was granted Study Leave by Ahmadu Bello University and then entered the Graduate School of The University of Texas. He married Mary Labija in 1965. Two daughters, Grace Elojo and Comfort Ojoma, were born in May, 1966, and May, 1968, respectively; a son, Arome, was born in October, 1970.

Permanent Address: c/o L.E.A., Ogodu
Ankpa P.O., Kwara State,
Nigeria

This dissertation was typed by Cathy G. Jost.